DILUTE SPECIES TRANSPORT IN NON-NEWTONIAN, SINGLE-FLUID, POROUS MEDIUM SYSTEMS

Minge Jiang

A technical report submitted to the faculty at the University of North Carolina at Chapel Hill in partial fulfillment of the requirements for the degree of Master of Science in Environmental Engineering in the Department of Environmental Sciences and Engineering in the Gillings School of Global Public Health.

Chapel Hill

2019

Approved by:

Cass T. Miller

Orlando Coronell

Jason D. Surratt

ABSTRACT

Minge Jiang

(Under the direction of Cass T. Miller)

Vast reserves of natural gas held in tight shale formations have become accessible over the last two decades as a result of horizontal drilling and hydraulic fracturing. Hydraulic fracturing creates patterns of fractures that increase the permeability of the shale. The production of natural gas from such formations has led to the U.S. becoming a net exporter of natural gas, lowered energy costs, and led to a reduction in coal-fired power generation, thereby reducing greenhouse gas emissions. The hydraulic fracturing process is complex and poses environmental risks, which are not clearly understood. Many fundamental questions remain to be answered before these risks can be clearly understood and analyzed. The difficulties result from the injection and attempted recovery of non-Newtonian fluids, which often include many species considered pollutants if encountered in drinking water, under gravitationally and viscously unstable conditions. This work investigates how species disperse in non-Newtonian fluids, which is a topic that has received scant attention in the literature. Dispersion is a deviation from the mean rate of movement, and it is caused by a combination of factors including molecular diffusion, and pore-scale velocity distributions, which are in turn affected by viscosity variations. A series of experiments were performed to quantify dispersion for porous medium systems consisting of non-Newtonian fluids flowing through a sand media. Non-Newtonian fluids included guar gum, which is a common additive used in hydraulic fracturing that leads to a shear-thickening dependence of the dynamic viscosity on the shear rate. The observed dispersion for the media under both Newtonian and non-Newtonian conditions was observed with dispersion increasing slightly for the non-Newtonian systems compared to dilute species transport in Newtonian systems. To further investigate the dispersion process, pore-scale modeling was performed using OpenFOAM. A non-Newtonian form of the momentum equation was solved along with a dilute species transport equation for a porous medium consisting of sphere packings similar to those for which laboratory experiments were performed. Simulated results were compared to the laboratory experiments and used to reveal mechanisms responsive for dispersion. The results of this work provide a means to improve fundamental understanding and mathematical models of flow and transport resulting from hydraulic fracturing.

ACKNOWLEDGEMENTS

On my way here today to finish this report, I have a lot of people whose support, advice, and help have been fundamental parts of my accomplishments in life. First of all, I want to sincerely thank my advisor, Dr. Cass T Miller, who gave me plenty of support, patience, guidance, and help during the last one and a half years at UNC-CH. He was incredibly patient to edit my writing repeatedly, helped me to improve my work, explained obscure professional terms to me, taught me theoretical essential knowledge about groundwater hydrology, and guided me into numerical methods and the scientific computation world. Without his help, I could not have finished this final report ahead of the original plan.

Furthermore, I would like to give special thanks to the members of Dr. Miller's research group: Christopher Bowers, Brittany Shepherd, Kelsey Bruning, Timothy Weigand, Christopher Fowler, and Pamela Schultz, who have helped me in areas ranging from housing to classes to research work throughout the time I have spent here. I am especially grateful to Christopher Bowers; without his support to teach me about the experiments and simulations, and his explanations of many hard-to-understand theories, I would not have been able to complete my report, or indeed to make it through this year and a half at all. I want to thank my committee members, Dr. Orlando Coronell and Dr. Jason Surratt; their classes were insightful and informative. It has been my honor to work with all of them.

Finally, I would like to thank my friend, Whitney Tevebaugh, who helped me a lot with my English writing and speaking, assisted me with moving, and even offered food to me when I was busy with research and study. I would like to thank my ex-girlfriend, Suki Ye, who is always there for me whenever I need. Without her support, I could not have survived at graduate school. I want to thank my country, China, for cultivating me and guiding me through my life.

TABLE OF CONTENTS

LIST OF FIGURES vii

LIST OF TABLES viii

LIST OF NOMENCLATURE ix

Roman Letters ix

Greek Letters ix

Mathematical Letters x

LIST OF ABBREVIATIONS xi

Chapter 1: Introduction 1

Motivation 1

Goal and Objectives 6

Chapter 2. Background 7

Natural Gas 7

Hydraulic Fracturing 9

Non-Newtonian Fluids 11

Mathematical Modeling 13

Representative Elementary Volume 14

Hydrodynamic Dispersion 15

Chapter 3. Methods and Materials 18

Experimental Methods 18

Materials 18

Column 19

Guar Gum 20

Tracer Tests 21

Simulations 24

Sphere Packing 25

OpenFOAM Simulation 26

Data Calculation and Analysis 35

Dispersion 35

REV 37

Peclet number 38

Reynolds number 38
Chapter 4. Results and Discussion 39
Column experiments 39
Breakthrough Curve..... 39
Hydrodynamic Dispersion 45
Advection-Diffusion Model Fitting..... 47
Peclet Number..... 49
Reynolds number 50
Simulation 51
Sphere Packing 51
Pressure Drop..... 52
REV 57
ScalarTransport 57
Advection-Diffusion Model Fitting..... 64
Chapter 5. Conclusion 68
Bibliography 71

LIST OF FIGURES

Figure 1. Schematic of Column-Pump Porous Medium System *20*
Figure 2. Schematic of Domain System *28*
Figure 3. DIW Tracer Tests Breakthrough Curve *40*
Figure 4. DIW Tracer Tests 95% Confidence Interval Breakthrough Curve *40*
Figure 5. 0.3% Guar Gum Tracer Tests Breakthrough Curve *41*
Figure 6. 0.3% Guar Gum Tracer Test 95%CI *42*
Figure 7. 0.5% Guar Gum Breakthrough Curve *42*
Figure 8. 0.5% Guar Gum Tracer Test 95% CI *43*
Figure 9. Post-DIW Tracer Test Breakthrough Curve *44*
Figure 10. Post-DIW Tracer Test Breakthrough Curve 95% CI *44*
Figure 11. Experimental Mean Breakthrough curve comparison *45*
Figure 12. Experimental Hydrodynamic Dispersion Comparison *46*
Figure 13. Experimental Mean Dispersion 95% CI *47*
Figure 14. Experimental Breakthrough Curve Fitting *48*
Figure 15. Analytical Hydrodynamic Dispersion Model Sensitivity *49*
Figure 16. Experimental Pe Number *50*
Figure 17. Picture of the Domain from ParaView *52*
Figure 18. Pressure Drop Varies with Different Spheres and Blocks *55*
Figure 19. Pressure Drop for 0.3% Guar Gum at v = 0.00005 m/s *55*
Figure 20. Average Pressure Drop per Length for 0.3% Guar Gum at v = 0.00005 m/s *56*
Figure 21. REV With Respect to Conductivity Under Different Domain Systems *57*
Figure 22. Simulation Breakthrough Curve at v=0.0005m/s, D_T=2.05E-10 ..... *58*
Figure 23. Simulation Breakthrough Curve at v=0.00005m/s, D_T=2.05E-10 ..... *59*
Figure 24. Simulation Breakthrough Curve v=0.000005m/s, D_T=2.05E-10 ..... *59*
Figure 25. Simulation 0.3% Guar Gum at v=0.0005m/s Breakthrough Curve *60*
Figure 26. Simulation 0.3% Guar Gum at v=0.000005m/s Breakthrough Curve *60*
Figure 27. Simulation 0.5% Guar Gum at v=0.00005m/s Breakthrough Curve *61*
Figure 28. Simulation Hydrodynamic Dispersion at different velocities *62*
Figure 29. Simulation Hydrodynamic Dispersion at Different D_T *63*
Figure 30. Simulation Breakthrough Curve Fitting *65*

LIST OF TABLES

Table 1. Column and Sand Data *39*
Table 2. Experiment Reynolds Number *50*
Table 3. Packed Domain Systems Data *51*
Table 4. Rheological Cross-Model Parameters for Guar Gum Solutions *53*

LIST OF NOMENCLATURE

Roman Letters

A	Area [L^2]
C	Concentration [M/L^3]
C_0	Initial concentration [M/L^3]
D_l	Longitudinal hydrodynamic dispersion coefficient [L^2/T]
D_m	Molecular diffusion coefficient [L^2/T]
g	Gravity acceleration [L/T^2]
K	Hydraulic conductivity [L/T]
l	Linear coordinate along the flow direction [L]
L	Length [L]
m	Cross power model fitting parameter
M	Mass [M]
n	Cross power model fitting parameter
N_s	Sphere number
P	Pressure [M/LT^2]
Q	Flow rate [L^3/T]
r	Radius [L]
t	Time [T]
T	Relative concentration in OpenFOAM simulation
$\boldsymbol{u}$	Flow velocity tensor with the order of two [L/T]
v	Darcy velocity [L/T]
$\bar{v}$	Average Darcy velocity [L/T]
V	Volume [L^3]
X	Mean diameter of particles [L]

Greek Letters

α	Courant number
α_l	Dispersivity of the porous medium [L]
$\dot{\gamma}$	Shear rate [T^{-1}]
ε	Porosity

μ Dynamic viscosity [M/LT]

μ_0 Dynamic viscosity at zero shear rate [M/LT]

μ_{Inf} Dynamic viscosity at infinite shear rate [M/LT]

μ_{log} Lognormal mean

ν Kinematic viscosity [L^2/T]

ν_0 Kinematic viscosity at zero shear rate [L^2/T]

ν_∞ Kinematic viscosity at infinite shear rate [L^2/T]

ρ Density [M/L^3]

σ^2 Lognormal distribution variance

τ Shear stress [M/LT^2]

ω Specific thermodynamic work per unit mass

Mathematical Letters

$\frac{C}{C_0}$ Relative concentration

dh Hydraulic head loss [L]

$\frac{dh}{dL}$ Hydraulic gradient

$erfc$ Complementary error function

$grad$ Gradient

MASS Mass [M]

Pe Peclet number

PV Number of pore volume passed through

PV_C Pore volume of the column [L^3]

Re Reynolds number

Re_0 Reynolds number at zero shear rate

Re_{Inf} Reynolds number at infinite shear rate

ΔP Pressure Drop [M/LT^2]

∇ Differential operator

LIST OF ABBREVIATIONS

100^3	Resolution blocks level at x-y-z as 120×100×100
200^3	Resolution blocks level at x-y-z as 240×200×200
300^3	Resolution blocks level at x-y-z as 360×300×300
400^3	Resolution blocks level at x-y-z as 480×400×400
500^3	Resolution blocks level at x-y-z as 600×500×500
3GG	3% by mass guar gum solution
5GG	5% by mass guar gum solution
95% CI	95% Confidence interval
DIW	Deionized water
EPA	United States Environmental Protection Agency
EIA	United States Energy Information Administration
OpenFOAM	The Open Source Field Operation and Manipulation
REV	Representative Elementary Volume
Tcf	Trillion cubic feet
Tcm	Trillion cubic meters

Chapter 1: Introduction

Motivation

Global primary energy consists of petroleum, natural gas, coal, nuclear energy and renewable sources. In 2018, the world primary energy production grew by 2.8% compared to the primary energy production in 2017, and the U.S. and China together made up 54% of this growth [1]. Global primary energy consumption grew 2.9% in 2018, the fastest growth rate since 2010, mainly driven by natural gas, which accounted for more than 40% of the total increase. Approximately 85% of this consumption was in the form of fossil fuels. Global natural gas production and consumption increased by 5.3% and 5.2% in 2018, respectively, and nearly half of the production growth occurred in the U.S. [2]. In the U.S., fossil fuel accounted for approximately 80% of energy consumption in 2018, with 31% of energy consumption provided by natural gas [3].

Fossil fuels will continue to play an important role in energy production and consumption in the coming decades around the world, even as the transition to renewable sources of energy continues [4]. A long-term projection report indicates that, without a dramatic shift in current climate policies, global energy consumption will grow 20%-30% from now through 2040, mainly driven by fossil fuels, especially natural gas [5]. Based on the evaluation of Tong et al. [6], in 2018, the world recoverable conventional oil and natural gas resources are 535 billion tons and 588.4 trillion cubic meters, respectively. In 2016, Wang et al. [7] assessed total global recoverable unconventional crude oil and natural gas resources, which are stored in

tight geological formations with low permeability, at an astonishing 442.1 billion tons and 227 trillion cubic meters, respectively. Both of these estimates document abundant conventional and unconventional hydrocarbon resources globally.

Hydrocarbon reserves are stored in two different ways and require different extraction technologies. The hydrocarbon resources that come from high-permeability formations, such as large fractures in sandstones or limestones, can be easily obtained by standard well and pumping technologies and are called conventional hydrocarbons. Alternatively, unconventional hydrocarbons are usually trapped in tight geological formations, such as shales, with low permeability and porosity, and cannot be extracted from the deposit by utilizing simple drilling and production techniques. The latest data shows that from 2016 to 2017, the proven crude oil reserves in the U.S. increased 19.5% to 39.2 billion barrels (bbl), equivalent to 5.73 billion tons. Moreover, the proven natural gas reserves increased by 36.1% to 464.3 trillion cubic feet (Tcf), equivalent to 13.15 trillion cubic meters (Tcm). It should be noted that the share of shale gas grew from merely 13.5% in 2008 to 66% in 2017, or about two-thirds of the total proven natural gas reserves [8]. The increasing importance of shale gas, or unconventional natural gas, is an influential trend in energy production and consumption, especially in the U.S.

Hydraulic fracturing, also known as fracking, is one of the most important extraction technologies in the fossil fuel industry since the late 1940's, and the primary method for unconventional hydrocarbon resource exploitation. Hydraulic fracturing has developed dramatically in the past few decades to enhance the production of hydrocarbon from tight formations, making it possible to produce shale gas

economically from unconventional reservoirs [9]. From 2004 to 2019, the production of shale gas in the U.S. grew from about 0.8 billion cubic feet (22.6 million cubic meters) per day to 3.0 billion cubic feet (85.0 million cubic meters) per day [10]. Though it is a fossil fuel that produces greenhouse gas when burned, natural gas emits approximately 50% less CO_2 than coal and about 28% less CO_2 than oil per unit of energy production [11], and it emits far less sulfur dioxide (SO_2), and nitrogen oxides (NO_x) than either coal or oil. The projection from EIA [12] in 2019 shows that, without significant changes to clean energy policies, annual energy-related CO_2 emission will fall 4% to about 5 billion metric tons from 2018 to 2050 in the U.S. as a result of a migration from the consumption of coal and petroleum to natural gas.

The practice of hydraulic fracturing is generally combined with horizontal drilling techniques, and the process includes several steps: (1) drilling and construction of wells vertically and then horizontally to reach the hydrocarbon reservoirs far below the surface; (2) injection of pressurized hydraulic fluids into the wells to exceed the fracture gradient of the shale needed to form permeable cracks for fluids; (3) production of petroleum and natural gas from the wells; and (4) maintenance of the well system and treatment and disposal of fluid waste [13]. Although hydraulic fracturing dominates the global production of natural gas, it has been a controversial technique since its introduction. Concerns about the potential impacts of hydraulic fracturing on the environment, especially on groundwater and surface water quality, have drawn considerable attention from the research community, the public, and government [14–20].

The primary concern regarding fracturing is related to the effects of hydraulic

fracturing fluids applied during the fracturing process on subsurface water quality. Hydraulic fracturing fluids are often a type of non-Newtonian fluid, which consists of sand, large amounts of water, and a mixture of toxic chemicals. Specific concerns related to the hydraulic fracturing process include leakage of fluids, unrecovered fluids seeping down into the reservoirs, and potential transport of toxic chemicals into groundwater systems, the ecosystem, and water supplies [21]. Such contamination from hydraulic fracturing is extremely difficult to identify and remediate. Many open research questions must be resolved before the environmental risks resulting from hydraulic fracturing can be clearly understood. Included in these open questions are the mechanics of transport phenomena in non-Newtonian fluids, which are the majority of fluids used in hydraulic fracturing.

Fluid characterization depends on a number of variables. Different fluids or materials have their own behavior patterns when subjected to stress, shear rate, velocity, deformation, and flow. Based on their viscosity characteristics, fluids can be classified as Newtonian or non-Newtonian fluids. Newtonian fluid remains at a constant viscosity as a linear function of shear stress and shear rate; water and gasoline are two examples. Non-Newtonian fluids are a group of materials, such as biological fluids, aqueous guar gum solutions, and suspensions, whose viscosity characteristics do not follow the classic Newtonian model [22]. As compared to Newtonian fluids, the viscosity of non-Newtonian fluids [23] has a non-linear correlation between the shear rate and shear stress. When the derivative of the shear stress with respect to the applied shear rate is positive, the fluid is defined as a shear-thickening fluid, for which the viscosity correspondingly increases as the shear rate grows. When the derivative

of the shear stress with respect to applied shear rate is negative, the fluid is called a shear-thinning fluid, for which the viscosity decreases as the shear rate increases.

In fluid mechanics, hydrodynamic dispersion is a factor that has been applied to describe the transport of solutes in fluids. In the 1950s, Dr. Geoffrey Ingram Taylor [24–26] published several papers about soluble matter dispersion in Newtonian fluids flowing through a tube under certain fluid conditions. Taylor derived a classic hydrodynamic model, known as the Taylor dispersion model. The Taylor dispersion model has been proven efficient to fit Newtonian fluids [27–29]. However, because of the unstable viscosity of non-Newtonian fluids, the Taylor dispersion model cannot accurately describe the behavior of non-Newtonian fluids or species transport in non-Newtonian fluids in porous media. The nature of species transport and dispersion in non-Newtonian fluids remains unclear, and additional research is warranted. The standard hydrodynamic dispersion model [30] from Taylor is based on mass conservation equations and simulates the behavior of species in Newtonian fluids; however, the hydrodynamic dispersion model for non-Newtonian fluids is uncertain, and this work aims to narrow this knowledge gap in non-Newtonian fluids. Utilizing the continuum method and the representative elementary volume concept, one can observe variations in species dispersion in a non-Newtonian fluid in porous media at the microscale level. These observations can then inform macroscale models of such systems. Promoting such fundamental understanding would enable advances in models used in a variety of fields including: hydrocarbon reservoir engineering, groundwater hydrology, chemical processing, and other areas in which flow phenomena exist in a porous media system.

Goal and Objectives

The goal of this work is to analyze dispersion of a dilute species in a non-Newtonian fluid for single-fluid-phase transport in a porous media system. The specific objectives of this work are: (1) to observe dilute species transport in an experimental porous media system that includes a non-Newtonian fluid; (2) to mathematically model species transport at the microscale for systems similar to those investigated experimentally; and (3) to compare experimental observations and simulated transport with regard to dilute species transport.

Chapter 2. Background

Natural Gas

Natural gas is one of the most common fossil fuels, naturally occurring deep beneath the surface of the earth. Like other fossil fuels, natural gas is made up of remnants of processes occurring under immense pressure and heat below the earth's crust for millions of years. Natural gas [31] consists of many different hydrocarbons, carbon dioxide, nitrogen, and water vapor, but the primary component of natural gas is methane (CH_4). Natural gas that is found in large fractures in permeable formations is called conventional natural gas, and natural gas that is found in fine-grained shale formations with low permeability is called unconventional natural gas, or shale gas. Natural gas occurrence is usually associated with petroleum deposits. In the 19th century, natural gas was considered a by-product of crude oil extraction and was burned off as waste from the petroleum field. However, in 2018, natural gas contributed 32% of U.S. primary energy production [32], a figure that keeps growing. With new extraction techniques and discoveries, the expansion of natural gas production, and especially the dramatic rise in shale gas production has remapped the U.S. energy landscape and turned the U.S. from a net energy consumer into a net producer.

Many qualities of natural gas make it an economical and relatively clean energy source. Natural gas has a higher caloric value (12,500 kcal/kg) than fuel oil (9,250 kcal/kg) or brown coal (3,500 kcal/kg) under standard conditions [33]. Natural gas also has fewer undesirable by-products emitted on combustion per unit energy than crude oil or coal [34], including sulfur, mercury, and particulates [35]. Although the powerful

greenhouse effect of methane [36], the simplest alkane and principal component of natural gas, and the leakage of natural gas from infrastructure [35] make its use controversial with regard to climate change and global warming, natural gas is still a relatively abundant, economical, efficient, and environmentally friendly fossil fuel worldwide [34,37]. Natural gas is widely used as a fuel for homes, power plants, industry, and automobiles. The typical efficiency of converting heat energy into electrical power in a power plant is 60% for a natural gas combined-cycle power plant, 42% for a petroleum-fired power plant, and 33% for a coal-burning power plant [34]. At the end of 2017, the net increase in proved natural gas reserves in the U.S. was 123.2 Tcf, about 3.49 trillion cubic meters (Tcm); this was a new record of total proved natural gas reserves, and the share of proved shale gas reserves increased to 66% of total U.S. proved natural gas reserves [8].

Shale gas trapped in a shale deposit or formation has become the primary source of natural gas production in the U.S. this century [38–40]. A shortage of crude oil and conventional natural gas in the late 1960s, along with an evolution in extraction methods made shale gas a significant energy source in fossil fuel production and consumption worldwide. Technological advancements made the extraction of shale gas economically viable. As one of the countries with the greatest proved natural gas reserves, the U.S. has a large amount of stored natural gas that has not yet been extracted. Prior to a few decades ago, these shale gas reservoirs were considered uneconomic targets, requiring difficult procedures to access. However, due to the development of hydraulic fracturing, these reservoirs are now both accessible and economical. According to EIA, shale gas accounted for approximately half of natural

gas production in the U.S. in 2017 [41]. Since extraction technology for natural gas hydrates, also known as methane clathrate, is still evolving, shale gas will play a significant role in the area of natural gas resources in the near future. Hydraulic fracturing technology is becoming increasingly important, and it is indispensable for exploiting shale gas reservoirs in the natural gas industry.

Hydraulic Fracturing

Hydraulic fracturing has become prevalent in crude oil and natural gas engineering in recent decades. Hydraulic fracturing [42] is an established and rapidly advancing technology that injects pressurized hydraulic fracturing fluids into targeted rock formations through production wells to create fractures and maximize productivity of petroleum and gas. Hydraulic fracturing forms cracks in permeable formations with fine grains, props these fractures open using sand or silica, and improves the permeability of tight shales artificially, allowing shale gas or petroleum to flow more easily out of the shale than before.

Horizontal drilling is a procedure that follows vertical drilling down into the subsurface. The horizontal portion of a well allows for a greater extent of a gas-containing region to be in close contact to the well, reducing transport distances needed for effective production. Hydraulic fracturing contributed 67% of the natural gas production and 51% of crude oil production in the United States in 2015, (EIA [43,44]). Since most of the shallower and more-accessible oil- and natural gas-bearing rock formations have already been exploited, hydraulic fracturing allows fossil-energy-mining technology deep into production formation layers previously considered uneconomic. Along with vertical and unconventional horizontal drilling methods, hydraulic fracturing has

spread as a popular technique to help the world access existing energy reserves.

The hydraulic fracturing process includes well construction, water acquisition, chemical mixing, pressurized injection, oil or natural gas extraction, and wastewater disposal and reuse [13]. Hydraulic fracturing fluids are injected under high pressure to open fractures in tight formations. The composition of fracking fluids varies with different types of fracturing, usually consisting of water, proppants which are solid materials such as sand, ceramic, and silica, and specific chemical additives, such as gels, guar gum, biocides, emulsifiers, and friction reducers. Industrial practice tends to choose more viscous fluids to carry more proppants, and such fluids are often non-Newtonian fluids. Some of the components of hydraulic fracturing fluids are biologically toxic, and the behavior of non-Newtonian fluids is difficult to model and predict.

The advent and rapid development of hydraulic fracturing has drawn substantial attention and debate from environmentalists, scientists, government, and the general population. Due to the intricacy of unconventional reservoirs and geological conditions, and the unclear attributes of hydraulic fracturing fluids, concerns have been raised regarding the risk posed by the initiation and propagation of fractures in shale formations and the potential resultant threats to groundwater aquifers. The possible environmental hazards of hydraulic fracturing include substantial water use, leaks and spills of hydraulic fracturing fluids, potential transport of fluids into groundwater resources, and other risks associated with operations and extractive activities [45,46]. Although there has been tremendous crude oil and natural gas produced through hydraulic fracturing technology and considerable research on

hydraulic fracturing techniques and applications, this process receives relatively little regulatory surveillance, and the impacts of hydraulic fracturing on surface water sources and groundwater remain unclear and infrequently studied.

In addition to lack of monitoring and regulation, scientific issues remain to be resolved before a mature level of understanding is achieved. One of these issues is related to the flow of non-Newtonian fluids, which are the typical hydraulic fracturing fluids, through porous media. Non-Newtonian flow through a porous medium system is often modeled using Darcy's law, which is not strictly applicable because it does not account consistently for the relationship observed between shear stress and shear rate that typifies a non-Newtonian fluid. Furthermore, the transport of individual dilute species in non-Newtonian fluids, such as is typical of many of the species of environmental concern, is also not well understood.

Non-Newtonian Fluids

In fluid mechanics [47], the force applied to a fluid parallel to the direction in which the fluid is moving per unit area is known as the *shear stress* (τ) [M/LT^2]. *Dynamic viscosity* (μ) is defined as the deformational resistance of a fluid to applied shear stress. When the shear stress exerted on a fluid is linearly proportional to the shear rate ($\frac{dv}{dy}$), the viscosity of the fluid is constant, and the fluid is said to be Newtonian. This relationship can be formulated as ***Eq. (1)***.

$$\tau = \mu \frac{dv}{dy} \qquad \textbf{(1)}$$

where μ is the dynamic viscosity of the fluid [M/LT].

The viscosity of Newtonian fluids remains constant at a given temperature, which means it is easy to measure the dynamic viscosity for such a fluid. Common Newtonian fluids include water, alcohol, gasoline, and mineral oil.

Fluids that do not follow Newton's law of viscosity are known as *non-Newtonian fluids*. Although many fluids are assumed to be Newtonian fluids for practical use, non-Newtonian fluids are more common and have very different behavior and properties than Newtonian fluids. In contrast to Newtonian fluids, the viscosity of a non-Newtonian fluid varies as a function of the applied shear stress or force. The behavior of a typical Newtonian fluid, such as water, depends on pressure and temperature. The behavior of a non-Newtonian fluid changes with flow conditions as a result of the dependence of dynamic viscosity on the rate of strain, in addition to the dependence on pressure and temperature. A typical example of a non-Newtonian fluid is ketchup: if one squeezes and shakes a ketchup bottle, it will pour out significantly faster than just turning over the bottle to wait for it to drop, because the ketchup's viscosity is altered when a stress is applied to it.

Non-Newtonian fluids can demonstrate various trends in dynamic viscosity as a function of the deformation rate, time, and composition, and there are four types of non-Newtonian fluids [48]. When the viscosity of a non-Newtonian fluid decreases with the increased shear rate, the fluid is called a *shear thinning* fluid, such as ketchup; when the viscosity increases with the increased shear rate, the fluid is called *shear thickening* fluid, such as oobleck. For time-dependent viscosity, if the viscosity of the fluid decreases with the length of time that stress is applied, then the fluid is defined as *thixotropic* fluid, such as glue; in contrast, if the viscosity of the fluid increases with

the length of time that stress is applied, the fluid is known as a *rheopexy* fluid, such as cream [49]. Because of the unique behaviors of non-Newtonian fluids, it is important to fully understand their properties in order to understand flow and transport phenomena in the porous medium systems in which they exist, such as in hydraulic fracturing applications.

Mathematical Modeling

Understanding of transport phenomena, engineering design, risk assessment, management, and policy related to natural gas recovery all depend upon a quantitative understanding of how mass, momentum, and energy are transported in porous medium systems [50–53]. This modeling can be performed at different length scales, two of which are especially important. At the microscale, the laws of continuum mechanics are reasonably well understood, but it is necessary to describe the precise location of each phase as a function of space and time. For natural systems at field scale this is not possible due to observational difficulties and computational limitations. Because of the challenges with microscale modeling, natural systems are usually modeled at the macroscale, where a point represents the centroid of an averaging region over all phases. The macroscale concept overcomes the challenges with microscale modeling, but raises issues regarding the appropriate form of the model and the size that a macroscale point needs to be for the model to be well behaved and meaningful. If the point is too small averaged quantities may be sensitive to the size of the averaging region. If the point is too large, natural variations may not be adequately resolved. The determination of this point size is often called the representative elementary volume (REV) problem, which is considered in the section

that follows.

Representative Elementary Volume

In order to derive a macroscale mathematical model to describe transport phenomena in a porous medium, Bear [30,54] applied a continuum approach that resolves the behavior of fluids inside a system in an averaged sense, which is referred to as the macroscale; the optimal size of this averaging region is a termed a representative elementary volume (REV). The partial differential equations for the mechanistic model then can be deduced using the REV point perspective. To define the size of REV, there are several principles that should be followed.

For any REV at point *P*, the length of the REV Δl_0 should be larger than the free path of molecules λ to avoid meaningless fluctuations of statistical variables in the molecular scale of magnitude, as well as smaller than a characteristic length L_0 to capture the valuable changes in the fluids; and this relationship is described as ***Eq. (2)***:

$$\lambda < \Delta l_0 < L_0; \tag{2}$$

Similarly, the time interval Δt_0 should be smaller than characteristic time T_0 to avoid information loss, and larger than the average free time [55] of a molecule. For porous medium domain system, to determine the size of REV in any point of the domain system, REV can be defined as a certain volume of the sphere ΔU_0, which is larger than one pore with a lower bound often taken as being on the order of tens of pores. The averaged macroscale properties of the system should be insensitive to the size of the REV, which is to say that a clear separation of length scales should exist between the microscale and the macroscale.

Based on the fluid continuum approach and REV, the meaningful average values of variables at any given REV provide a basis to develop mechanistic ways to observe physical, kinematic, and dynamic characteristics at the macroscale. Some useful macroscale characteristics include porosity, hydraulic conductivity, viscosity, diffusion, and hydrodynamic dispersion. Hydrodynamic dispersion is of special interest in this work, because little work has been done to characterize this process for non-Newtonian flows.

Hydrodynamic Dispersion

In recent decades, many groundwater investigations have emphasized groundwater degradation, especially due to petroleum recovery [56–59]. Because of the unique properties of non-Newtonian fluids, fluids commonly used in the oil industry, understanding and quantitatively describing flow and transport phenomena for non-Newtonian fluids in the subsurface is important. Non-Newtonian fluids applied during hydraulic fracturing contain a variety of dissolved species when injected into target formations, and the potential mixing with petroleum, shale gas, and native groundwater further complicates the mixture [60,61]. Models for fluid motion during hydraulic fracturing are needed, and the description of species' transport in non-Newtonian fluids through porous medium is also necessary.

In groundwater hydrology and fluid mechanics, hydrodynamic dispersion [62] has been used to denote the combination of mechanical dispersion in the fluid due to the fluctuations from mean advective transport and the transport of the fluid species due to molecular diffusion. Advection is typically the term used to denote the rate of transport due to the mean velocity of the fluid. Freeze and Bear [62,63] used the

concept of hydrodynamic dispersion to describe deviations from the mean rate of transport resulting from advective transport. Hydrodynamic dispersion can be observed by the distribution of the velocity of the species in the fluids. While the solute moves with the fluid, it tends to spread out in the transverse and longitudinal directions based on mechanical dispersion and molecular diffusion. Freeze [63] explained that the mechanical dispersion, or hydraulic dispersion, occurs because of three mechanisms: the drag force caused by the roughness of the pore surface; the variation of pore sizes in the flow path; and the tortuosity due to the presence of solid particles that obstruct flow. Generally, the molecular diffusion is small enough to be negligible except when the flow velocity is small.

Taylor [24] studied the hydrodynamic dispersion of a species for single fluid flow through a cylindrical tube. Specifically, the effect of an unresolved microscale velocity distribution along with molecular diffusion was related to the mean rate of macroscale flow. Taylor developed an approximate solution that accounted for the unresolved microscale velocity distribution on the spread of a dissolved species. The velocity of the species near the wall of the cylinder is close to zero, and the velocity of the species in the center path reaches its maximum value. If one examines any cross-section in the cylinder that is perpendicular to the direction of the flow path, the integral of the velocity of the species at that face would be a constant and equal to the average velocity when viewed at the macroscale.

For porous medium systems, the situation is more complicated. Compared to a cylindrical tube without medium, fluid flowing through a column packed with a porous medium results in fluid flow around the particles of the medium, which further leads

to additional components of hydrodynamic dispersion compared to Taylor's pipe system. Mathematical models for species dispersion in a Newtonian fluid in a homogeneous, isotropic porous medium have been well established. However, most porous media are not homogeneous, and some of the fluids we care about are not Newtonian fluids. Solute dispersion in such stochastic media has been the focus of considerable research over the last few decades. More work is also needed for understanding dispersion in non-Newtonian fluids.

For the purpose of developing a mechanistic solution for species in non-Newtonian fluids, models based upon the conservation of mass, momentum, and energy are often used. A set of partial differential equations can be derived from conservation equations. However, these equations have more unknowns than the number of equations, leading to solvability issues. Therefore, closure relations such as Darcy's law are used to render the models solvable. Hydrodynamic dispersion is one such closure relation. While a useful form has been established for homogeneous porous media and Newtonian fluids, the correct form of the hydrodynamic dispersion closure relation for non-Newtonian fluids is an open question. Dispersion can be investigated using either laboratory experiments or mechanistic mathematical models.

Chapter 3. Methods and Materials

The overall goal of this work was to advance understanding of dilute species dispersion in non-Newtonian fluids flowing through porous medium systems. A combination of experimental and modeling methods was used in this work. A column system packed with sand was used to conduct a series of laboratory dispersion tracer tests; a microscale mechanistic model was implemented to model dispersion for a set of domain systems; and comparisons were then made between the experimental observations and the mechanistic modeling results. The sections that follow detail the approaches taken in this work.

Experimental Methods

Materials

The Newtonian fluid used in the experiments was deionized water (DIW), which was produced from a Dracor Water System (Durham, NC) with ultra-purification procedures using distilled water from UNC. Non-Newtonian fluids were made up from guar gum powder (Grade S-4500-G, Synthetic Natural Polymers, Inc. Durham, NC) dissolved in DIW, along with sodium azide (NaN_3, reagent grade, Sigma Aldrich) [64] to prevent biodegradation of the fluid system. The dilute species that was investigated was tritiated water (American Radiolabeled Chemicals, Inc.), with a portion of tritium (^3H) as the hydrogen atoms in water molecules added as a tracer to monitor its dispersion in Newtonian and non-Newtonian fluids flowing through porous medium systems. Tritiated water was pre-diluted by former users in the laboratory. Tritium is nonreactive, and has a relatively long half-life of 4,500 $\pm$ 8 days (around 12.3 years) and low radiation energy [65], which makes it a perfect tracer in laboratory tracer

experiments for fluids. Tritiated water was pre-diluted before it was added to DIW to produce a DIW-tritiated water solution. The density of the DIW and guar gum solutions were tested in the density meter DMA 48 (Anton Paar USA Inc.) at room temperature.

Column

A vertical column porous medium system (***Figure 1***) was designed to pump fluid through a porous media at the bottom of the column, and outflow samples were collected at the top in a designed time sequence. The column was packed with 20/30 Accusand (Unimin Corporation, USA) with an air vibrator (Syntron, USA) to compress the sand packing, and the diameter distribution and mean radius of the sand were collected by laboratory colleagues Scott C. Hauswirth and Christopher A. Bowers [66], whose paper is under review. The length and diameter of the column packed with sand were measured and recorded, with density of the sand used to calculate the porosity of the column porous medium. The inlet and outlet openings of the column on both sides were closed with plugs with a middle hole to connect the inside and outside of the domain system with plastic tubes. A syringe pump (Harvard Apparatus, USA) was also connected to the column with plastic tubes and three-way and two-way plastic valves to control the flow. CO_2 (Industrial grade, Airgas) was injected into the column for 30 minutes to push air bubbles out of the system completely, then sufficient DIW was pumped with a constant flow rate into the system to saturate the sand thoroughly and prepare the system for dispersion testing. Before every tracer test, the inlet connection lines were cleaned and saturated with the same target fluids accordingly.

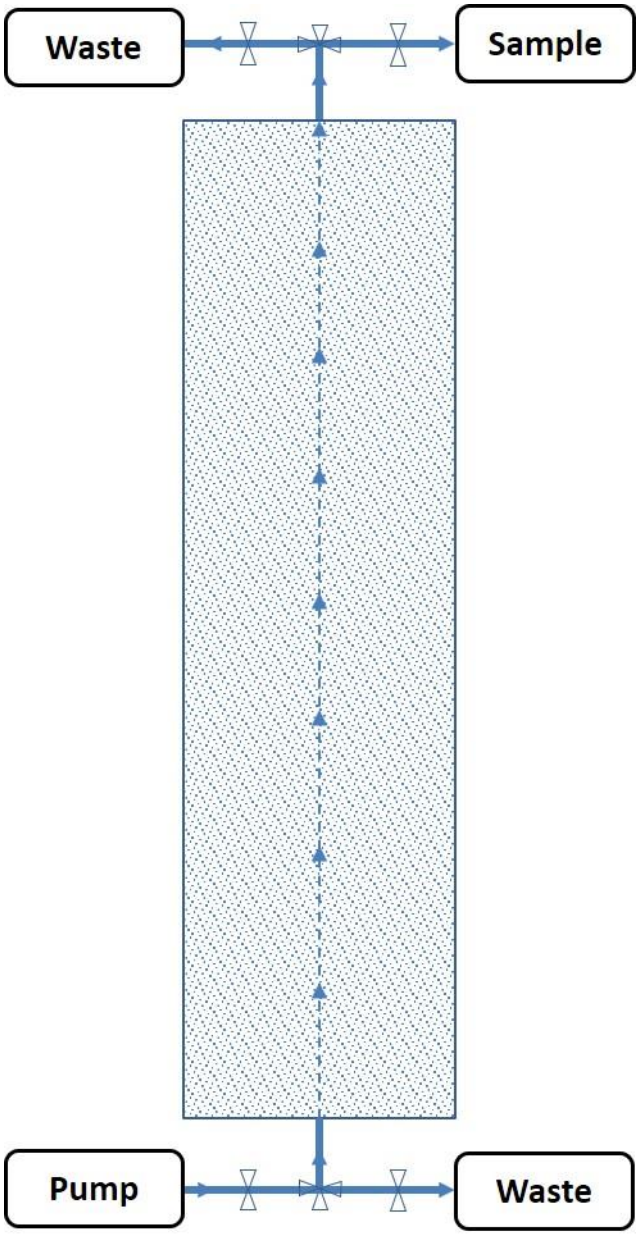

Figure 1. Schematic of Column-Pump Porous Medium System

Guar Gum

Guar gum [67] is commonly and economically applied to produce non-Newtonian fluids in hydraulic fracturing. Guar gum powder is produced from the endosperm of seeds from the guar plant, also known as the cluster bean. Due to the physical properties of guar gum as a galactomannan polysaccharide, dissolved guar gum powder in water forms hydrogen bonds with water molecules and is broadly used as an additive in pharmaceuticals, textiles, and food production. Specifically, guar gum is

used as a thickener and stabilizer in the petroleum and natural gas industries [68].

Guar gum powder was weighed and dissolved in DIW, DIW-tritium solution, along with approximately 1 g sodium azide, diluted to 1 kg in total. The DIW-tritium solution was further diluted about 100 times from the pre-diluted tritiated water based on the purchased tritium. The mixture was then mixed at the highest speed in an electric blender (Better Chef) for 30s and transferred into sealed glass containers after the mixing was finished. Then the mixture was stirred slowly with a magnetic stir bar in a magnetic stirrer (Thermix, Fisher Scientific) for about 24 hours until the guar gum was fully dispersed. After that, the mixture was transferred into sealed plastic centrifuge tubes and centrifuged for 30 minutes at 3100 R/min at 15℃ in a ventilated centrifuge (Marathon 21/R Ventilated Centrifuge, Fisher Scientific) to separate the potential uneven insoluble ingredients of the mixture. After centrifugation, the upper solution was homogenous and was collected as 0.05%, 0.1%, 0.2%, 0.3%, 0.4%, and 0.5% guar gum solutions by mass, or guar gum tritium solutions if the DIW-tritium solution was used to dissolve the guar gum powder. Before the solutions were injected into the column, the DIW, DIW-tritium, guar gum, and guar gum tritium solutions were degassed through a wall vacuum system in the laboratory to prevent air bubbles from moving into the column system and maintain the saturated status of the domain.

Tracer Tests

Tracer tests were performed by observing the transport of tritium in either DIW or guar gum solutions to quantify dilute species dispersion in both Newtonian and non-Newtonian fluids. For the non-Newtonian fluids, the concentration of guar gum was also a variable that was controlled. All experiments were run with a more viscous solution displacing a less viscous solution, which was needed for stability of the

displacement pattern.

DIW Up-Tracer Test: The plastic lines that connect the column with the pump were cleaned and pre-saturated with a DIW-tritium solution. The DIW-tritium solution was pumped at a flow rate (*Q*) of 40 mL/min (a velocity closes to general groundwater velocity [69–71]) into the column pre-saturated with DIW starting at a certain time (t=0) to replace DIW in the column. Outlet samples were then collected during the whole tracer test from the top of the column into 20 mL disposable scintillation vials (Fisher Scientific) at discrete and constant time intervals. The tracer concentration exiting the column *C=C(t)* is referred to as a breakthrough curve. We assumed and verified that after 1.6 pore volumes of the column of pumping the DIW-tritium solution, the breakthrough curve reached steady-state, and we stopped the pump and sample collecting. The steady-state concentration was verified by sequential sampling. This experiment was designated the up-tracer test, as the radioactivity in the column increases during the experimental period as a function of time.

DIW Down-Tracer Test: After the up-tracer test was completed; the column was saturated with DIW-tritium solution. The syringe pump then was refilled with DIW, and the plastic lines that connect the pump and the column were cleaned and pre-saturated with DIW. We started the pump at a certain time (*t=0*) to inject DIW to displace the DIW-tritium solution in the column, and we repeated the experimental steps as in the up-tracer test in the same discrete and constant time intervals. This experiment is called a down-tracer test because the radioactivity of the fluid in the column is decreasing with time during the experiment. Both the up-tracer test and the down-tracer test can be used to observe the macroscale dispersion in the system.

Guar Gum Tracer Test: For the guar gum tracer test, the column was first saturated with DIW. The guar gum solutions of interest were at concentrations of 0.3%, and 0.5% by mass. We picked these two specific concentrations of guar gum solution based on some pre-research data from coworkers in the group in order to detect a clear difference between Newtonian fluid and non-Newtonian fluid. When the concentration of guar gum is small, the difference between the guar gum solution and DIW is insignificant. In order to saturate the column with 0.3% guar gum solution, we used a step-up saturating procedure, which means the column was saturated step-by-step, first with 0.05%, then 0.1%, then 0.2%, and finally with 0.3% guar gum solution. The purpose of the step-up saturating procedure was to minimize the potential unstable flow inside the column system. After the column was saturated with 0.3% guar gum, the same up-tracer test procedure was followed, in which a guar gum tritium solution displaced a guar gum solution void of tritium, and outlet samples were taken in the same time sequence as DIW tracer tests to track the relative radioactive concentration in the output fluid. For the down-tracer guar gum tracer test, a guar gum solution void of tritium displaced the resident guar gum-tritium solution, and the same down-tracer samples were taken to observe the variation of the tracer in the output fluid. Experiments were conducted with 0.3% and 0.5% guar gum solutions separately, with the same step-up saturating procedure to saturate the column ahead of the experiments.

Post-DIW tracer test: After the guar gum tracer experiments were performed, the column was flushed with decreasing concentrations of guar gum solution void of tritium, and eventually DIW, the opposite step-down procedure to the saturating

process. At least ten pore volumes of DIW were circulated to flush the guar gum from the system before the post set of DIW tracer tests were performed. Following the flushing procedure, the post-DIW tracer tests were performed with the same steps as the DIW tracer test, and the same output samples were collected. The purpose of the post-DIW tracer tests was to verify the column after conducting several guar gum tracer tests.

Sample analysis: The samples collected from the tracer tests were combined with 8 mL liquid scintillation cocktail (Scintanalyzed, ScintiSafe Gel, Fisher Scientific, NC) and 1 mL of ethanol (200 proof, Decon Laboratories, Inc.) in sample vials. The liquid scintillation cocktail was used to enhance the long-term stability of the samples, improve counting efficiency, and reduce the contact time required for the radioactivity detector during analysis [72–74]. The mixture was sealed and shaken by hand immediately. The samples were then evaluated using a Tri-Carb 1900 TR Liquid Scintillation Analyzer (Packard Instrument Co Inc, USA). Samples were analyzed in triplicate, and the mean value of the three results for each sample were used for data analysis. Tracer tests were repeated at least two times for each concentration of guar gum solution, DIW tracer test, and post-DIW tracer test.

Simulations

Simulations consisted of four sections: the generation of media, the generation of meshes, the simulation of the non-Newtonian fluid field, and the simulation of the tracer transport in non-Newtonian fluid flowing through porous medium. The media was generated by a specific sphere packing code [75] from former research group members with different sphere numbers. The rest of the three simulations were

conducted with OpenFOAM applications to generate the meshes and blocks for the domain in order to obtain REV, simulate the saturating processes of the medium domain with non-Newtonian fluid, and simulate the transport of dilute species in non-Newtonian fluid passing through the pre-saturated domain system.

The first section allowed us to achieve domains with different sphere numbers and target porosity. The second and third sections provided data to analyze and optimize the better domain system and examine REV for the transport simulation. The last section permitted us to observe the variation of the tracer transport in non-Newtonian fluid passing through porous medium, obtaining microscale to macroscale data to study the hydrodynamic dispersion of non-Newtonian fluids in a single fluid, porous medium system. The outcome data were compared with the laboratory experimental data to evaluate and verify the hydrodynamic dispersion of non-Newtonian fluids in porous medium systems, as well as our research methods. The sphere packing code ran at a local workstation, and OpenFOAM applications were executed in the Dogwood cluster, a Linux-based computing system, at the University of North Carolina at Chapel Hill.

Sphere Packing

To generate the media, sphere packing was used to pack the domain with randomly generated hard spheres, with lognormal distribution of the size of spheres. The model of packing impacts the porosity of the media and the distribution of the particles, as well as the spheres, and therefore the behaviors of fluids and the domain system. This work applied Sphere Packing code from our group members [75,76] for random packing of incompressible spheres, with number of spheres N_s set as 1000, 2000, 3000, 4000, and 5000, as the sphere domain used for the following OpenFOAM simulation.

The initial porosity was 0.8, and target porosity was 0.36; the lengths of the domain in each of three-dimensions were the same for any one of the sphere domains and were specified by the expected volume of the lognormal packing as shown in ***Eq. (3)***. The lognormal distribution variance σ^2 was 0.004318914893.

$$\frac{4\pi N_s}{3}E[r^3] = \frac{4\pi N_s}{3}\exp\,(3\mu_{log} + \frac{9}{2}\sigma^2); \qquad \textbf{(3)}$$

where μ_{log} is the lognormal mean and r is the radius of sphere [L]. Since it is not possible to specify μ_{log}, σ^2, and porosity ε independently, we specified certain σ^2 and the target porosity, after which the value μ_{log} can be approximated based on these two data. The mean diameter of the spheres was the same as the mean diameter of sand used for the laboratory column-pump system; the mean radius of the spheres can be calculated by ***Eq. (4)***:

$$\bar{r} = \exp\,[\mu_{log} + \frac{\sigma^2}{2}]; \qquad \textbf{(4)}$$

The generated domain systems were applied in the OpenFOAM simulations described below.

OpenFOAM Simulation

The Open Source Field Operation and Manipulation (OpenFOAM), a popular open-source mathematical methods C++ library, was introduced to conduct computation for dilute species dispersion of Non-Newtonian fluids in the Linux-based system. Here we used the OpenFOAM User Guide (Version 6) [77] from the OpenFOAM source website to guide the simulation processes and *ParaView* to visualize and analyze some of the results of the simulation.

Pre-processing: Mesh generation

The pre-processing was the application of a specific mesh generator in OpenFOAM, *snappyHexMesh*, to create hexahedra (hex) and split-hexahedra (split-hex) for the three-dimensional meshes in Stereolithography (STL) or tri-surfaces. By iteratively refining the existing meshes generated through *blockMesh* and morphing the refined meshes to the surfaces of STL, *snappyHexMesh* created fine meshes with variable refinement levels to fit onto a given geometry. In general, the higher the refinement level, the more accurate the generated mesh will be, but the calculation processes for the computer to solve will be significantly larger and time-consuming. The *snappyHexMeshDict* dictionary provided a place to adjust the parameters of *snappyHexMesh*.

Under *system* directory, the application *blockMesh* was applied to generate blocks in three-dimensions on an x-y-z plane. The boundaries and initial conditions and other fields can be set up through different system data files. *DecomposeParDict* decided the number of decomposed blocks of the domain. *ControlDict* was responsible for control of time, such as the beginning and end of run time, time interval, and reading and editing field data. *decomposePar* was the application used for parallel processing in research computing, followed by *reconstructPar* to reconstruct the mesh fields.

blockMesh builds the mesh with blocks, and the different blocks number will impact the accuracy of the approximate solution for the partial differential algebraic equations (PDAE) and calculation counts. Eventually, the sphere domains with different sphere numbers were refined to 100^3 (x-y-z as: $120 \times 100 \times 100$, same sequence for following blocks), 200^3 ($240 \times 200 \times 200$), and 300^3 ($360 \times 300 \times 300$) blocks for most of the sphere domains, and 400^3 ($480 \times 400 \times 400$), 500^3

(600×500×500) blocks for selected domains. The difference in the x-axis is because the domains were rectangular, and because of the two reservoirs in two sides of the domain, the inlet and outlet, which were used to make sure the flow had the same velocity and direction when it encountered the sphere domains. The schematic of the domain system is shown in ***Figure 2***.

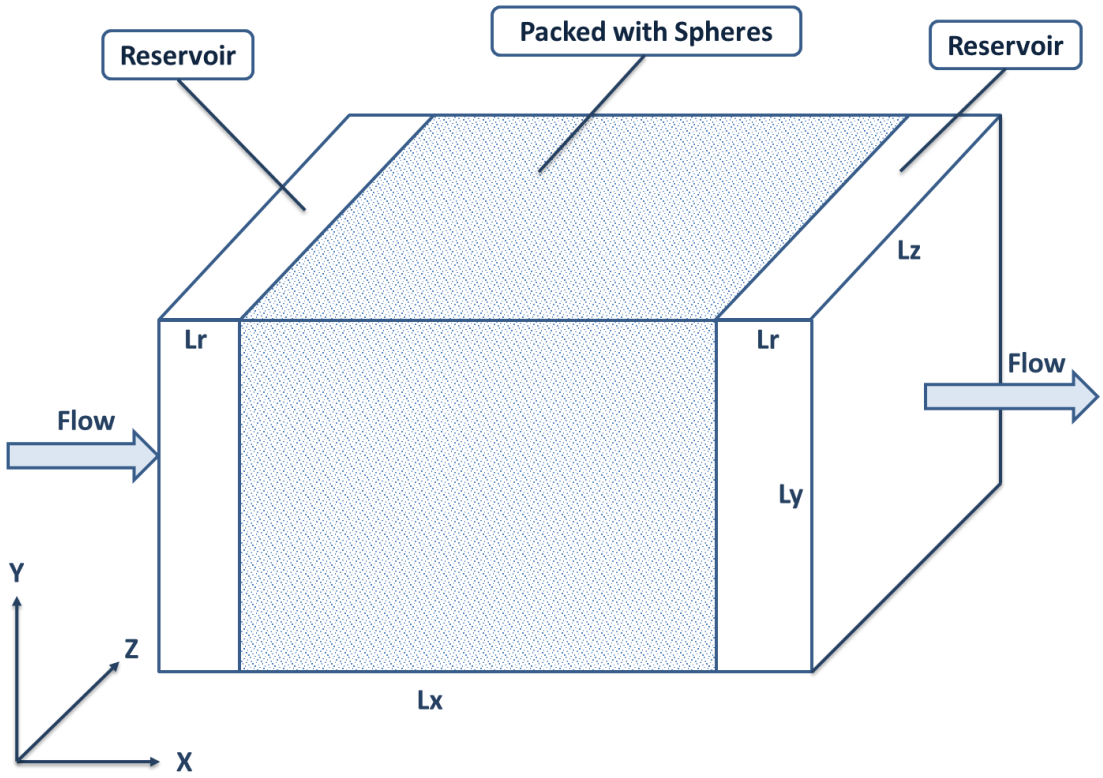

Figure 2. Schematic of Domain System

The lengths of the entire domain follow ***Eq. (5)***, and L_0 is the packed domain length derived from Sphere Packing; L_r is the length of the reservoir. The packed area of the entire domain is a cube, but because of the existence of the two reservoirs, the entire domain is a cuboid.

$$L_x = 1.2L_y = 1.2L_z; L_y = L_z = L_0; L_r = 0.1L_0; \quad \textbf{(5)}$$

Because of the reservoirs, the actual porosity of the domain was not the same as the initial porosity from sphere packing. The actual pore volume of the entire domain

system was collected by *checkMesh*, and was used to calculate the actual porosity of the entire domain system.

Non-Newtonian fluid field

After the execution of *snappyHexMesh*, the next step was *nonNewtonianIcoFoam* and the following post-processing. The *nonNewtonianIcoFoam* solver was used to solve the incompressible laminar flow movement for non-Newtonian fluids. For *IcoFoam* [78], it is a specific numerical method code that was designed to solve incompressible laminar Navier-Stokes equations [79–81] for viscous fluids by using Pressure-Implicit with Splitting of Operators (PISO) algorithm [82,83]. Navier-Stokes equations are a continuum with a set of partial differential equations derived from the momentum conservation equation for the viscous fluid system at the scale of interest (microscale here) by applying Newton's second law as a closure relation. Navier-Stokes equations include the pressure term and the stress applied on the fluid to simulate the unstable viscosity of the non-Newtonian fluid's movement specifically, and they have been widely applied in fluid mechanics, engineering, and other fluid scientific areas. PISO is an improved algorithm based on the SIMPLE algorithm by Issa [84] to calculate pressure-velocity for Navier-Stokes equations with larger time steps and accordingly less computational effort. The incompressible Navier-Stokes equation is as follows ***Eq. (6)*** [85]:

$$\frac{\partial \boldsymbol{u}}{\partial t} + (\boldsymbol{u} \cdot \boldsymbol{\nabla})\boldsymbol{u} - \nu \boldsymbol{\nabla}^2 \boldsymbol{u} = -\boldsymbol{\nabla}\omega + g; \qquad \textbf{(6)}$$

where, $\boldsymbol{u}$ is the flow *velocity tensor* with the order of two [L/T]; $\boldsymbol{\nabla}$ is the differential operator; ν is *kinematic viscosity* [L^2/T]; ω is specific thermodynamic work per unit

mass; and g is the gravity acceleration [L/T^2]; $\nabla\omega$ is estimated by ***Eq. (7)***:

$$\boldsymbol{\nabla}\omega \equiv \frac{1}{\rho_0}\boldsymbol{\nabla}p = \boldsymbol{\nabla}(\frac{P}{\rho_0}); \tag{7}$$

where ρ_0 is the uniform density of the fluid for incompressible fluid (here we assume the density variation is negligible); and p is the pressure [M/LT^2]. The Stokes's stress constitutive equation for incompressible viscous flow is ***Eq. (8)***:

$$\boldsymbol{\tau} = \mu(\boldsymbol{\nabla u} + \boldsymbol{\nabla u^T}); \tag{8}$$

where $\boldsymbol{\tau}$ represents the shear *stress tensor* [M/LT^2]; and μ is *dynamic viscosity* [M/LT]. The relationship between *kinematic viscosity* and *dynamic viscosity* can be formulated as ***Eq. (9)***:

$$\nu = \frac{\mu}{\rho}; \tag{9}$$

Substituting ***Eq. (7-9)*** into ***Eq. (6)***, the partial differential equations can be solvable with boundary conditions. To solve these complicated partial differential equations with respect to three-dimensions and time, we usually apply numerical methods to solve for the approximate solution within acceptable error. Navier-Stokes first can be discretized by the finite volume method, then in each time step, the PISO algorithm [82] takes the discretized equations with initial predict and boundary conditions to compute the velocity field and mass fluxes at the blocks faces from the *snappyHexMesh* step, and solve for pressure in blocks in the domain. Then mass fluxes and velocities are corrected based on the newly solved pressure field, and the boundary conditions are updated. These steps are repeated until the computational error is smaller than the acceptable error to convergence. After the iterations in one time step are finished, the time step increases and the iteration repeats again until the

time step reaches the set end time. The PISO algorithm is suitable for resolving velocity-pressure problems.

In the first set of *nonNewtonianIcoFoam* simulations, we tested each domain system from the *snappyHexMesh* step with a constant velocity ($v = 0.00005\ m/s$) (a velocity closes to the velocity used in experimental tracer tests and the general groundwater velocity) and the viscosity data for 0.3% guar gum solution by mass, collected pressure drop data for each domain system, and analyzed the data. This allowed us to evaluate REV based on the conductivity of the domain system, and to select the appropriate domain system for the transport simulations.

Specifically, we took the *polyMesh* solution data from *snappyHexMesh* for each sphere packing domain to the non-Newtonian solver and solved for pressure drop data with given boundary conditions. After running the same *decomposePar* to decompose the meshes, *nonNewtonianIcoFoam* was run in parallel to solve the non-Newtonian fluids passing through the porous medium, and *reconstructPar* for reconstruction in time sequence. The post-processing uses *patchAverage,* which solves for pressure drop for the whole domain at different time stamps. The variation of the pressure drop on the whole domain with respect to time can be evaluated if the domain system is steady-state. This step is the counterpart of the saturation process in the laboratory tracer tests.

A difference in *controlDic* is that courant number α must be smaller than 1 according to the following ***Eq. (10)*** [77]:

$$\alpha = \frac{\delta t}{\delta x}|v| < 1; \qquad \textbf{(10)}$$

in which δt represents *deltaT*, δx is the size of the cell, and $|v|$ is the velocity. Based on this equation, α can be adjusted by manipulating δt and δx to make sure it obeys the rule. The courant number also can be found from the *nonNewtonianIcoFoam* output log to examine any error and adjust the setting accordingly.

Other dictionaries, like *fvSchemes* and *fvSolution* dictionaries in *system* directory, were not needed to edit or change any parameter, and therefore are not discussed. Physical properties, such as Reynolds number and velocity, were assigned by *transportProperties* dictionary.

In the second set of *nonNewtonianIcoFoam* simulations, we took the selected domain system, then assigned different velocities ($v = 0.0005\ m/s;\ 0.00005\ m/s; 0.000005\ m/s$) respectively to three viscosity data: DIW, 0.3% and 0.5% guar gum by mass solutions separately on the domain system. We then ran *nonNewtonianIcoFoam* again to acquire velocity data for the saturated steady-state domain systems for the following transport simulation. The rheological measurements of the three viscosity data were investigated by laboratory colleague P.B. Schultz who applied a stress-controlled rheometer with a temperature-controlled plate and Rheology Advantage Instrument Control software program to analyze the measurements of viscosity at different shear rates for every guar gum sample. The cross-power law model used for kinematic viscosity for non-Newtonian fluids in OpenFOAM computing is ***Eq. (11)***:

$$\nu = \nu_\infty + \frac{(\nu_0 - \nu_\infty)}{1 + (m\dot{\gamma})^n}; \qquad \textbf{(11)}$$

where, ν_0 and ν_∞ are the kinematic viscosity at zero shear rate and infinite shear rate,

respectively; m and n are two fitting parameters; and $\dot{\gamma}$ is the shear rate.

ParaView was ultilized to visualize the domain system. Because the system is too large for the local workstation to do the processes for *ParaView*, *ParaView* was executed in the Longleaf cluster [86], another Linux-based computing system at the University of North Carolina at Chapel Hill, used particularly for a single compute host that requires large workloads.

Species Transport

The *scalarTransportFoam* application [87] from OpenFOAM was used to solve species transport equations for the concentration data with the specified velocity field data from *nonNewtonianIcoFoam*. *scalarTransportFoam* typically evaluates the approximate solutions for scalar convection-diffusion problems under certain boundary conditions. Here the boundary conditions are the fixed value of concentrations of species at the inlet ($T_0 = 1$) and zero gradient at the outlet of the domain system. The convection-diffusion equation solved by the *scalarTransportFoam* application is ***Eq. (12)***:

$$\frac{\partial T}{\partial L} + \boldsymbol{\nabla} \cdot (\boldsymbol{U}T) - \boldsymbol{\nabla}^2 (D_T T) = 0; \qquad \textit{(12)}$$

in which T represents the transported scalar with zero order, here the relative concentration of the species $\frac{C}{C_0}$; $\boldsymbol{U}$ is the velocity vector of the fluid; and D_T is the molecular diffusion coefficient divided by the density of the fluid. In *scalarTransportFoam* solver, the molecular diffusion coefficient and the fluid density are assumed as constants. Since the longitudinal direction is the direction of interest, the velocity of flow is in the longitudinal direction. The numerical method applied to

resolve approximate solutions for the transient transport equations is the finite volume method, the same as *nonNewtonianIcoFoam*.

The selected domains were applied in *scalarTransportFoam* after solved by *nonNewtonianIcoFoam* with different velocities and concentrations of the guar gum solutions. The velocity vector data was specified to the *scalarTransport* directory, along with the *polyMesh* data. We assigned the $D_T = 2.05E - 10$ according to two studies [88,89] in *transportProperties* dictionary, and set another $D_T = 0$ as a comparison.

Each of the entire domains was decomposed to a certain number of small domains, then the transport of species was computed in parallel at a certain time interval in the Dogwood cluster, and the transient relative concentration and time stamp were calculated and recorded by *reconstrucPar* and *postProcessing* applications. The relative concentration variations with respect to time were collected for the following analysis. The same *system* directory was used to adjust parameters for the simulation to run efficiently and appropriately.

Dogwood and Longleaf Clusters

The Dogwood cluster and Longleaf cluster [90] at the University of North Carolina at Chapel Hill are both Linux-based scientific computing systems that are available for students, faculties, and other researchers around campus to use for free. The Dogwood cluster has over 11,000 computing cores, large scratch disk space, and high-speed bandwidth to provide outstanding computing equipment for large, parallel MPI, or hybrid scientific programming models. The cluster uses Intel Xeon Skylake and Phi processors to comprise nodes, and each node includes 44 cores and 512 GB memory

to form different partitions to satisfy different requirements of the computational work. SLURM is used to manage resources and provides fair-share algorithm job management. secure shell (SSH), the submission script, and installation of applications and modules. Researchers are able to connect to the cluster and run programming models in Dogwood.

In contrast, the Longleaf cluster emphasizes accumulated jobs that require only a single compute host for each one of the jobs. Longleaf provides about 6500 compute cores, large memory, and scratch disk space. The same SLURM and SSH are used for job management and connections.

Data Calculation and Analysis

Dispersion

In order to develop mathematical equations to describe the transport of species in non-Newtonian fluid through porous medium, mass conservation is a typical approach that is introduced to qualitatively illustrate this physical transport process, see ***Eq. (13)***:

$$MASS_{in} - MASS_{out} \pm MASS_{reaction} = MASS_{net\ change}; \quad \textbf{(13)}$$

in which *MASS* represents the mass of the solute in and out of the domain system, and the mass of solute reaction in the system, as well as the net change of the mass of solute within the domain system.

For nonreactive species, with homogeneous, isotropic, pre-saturated medium, the one-dimensional mathematical hydrodynamic dispersion equation is expressed as differential ***Eq. (14)*** [63,91]:

$$D_l \frac{\partial^2 C}{\partial l^2} - \bar{v} \frac{\partial C}{\partial l} = \frac{\partial C}{\partial l}; \quad (14)$$

where D_l is the longitudinal hydrodynamic dispersion coefficient [L^2/T]; $\bar{v}$ is the average flow velocity in longitudinal direction [L/T]; l is the linear coordinate along the flow direction [L]; and C is the solute concentration [M/L^3]. The hydrodynamic dispersion coefficient can be formulated as ***Eq. (15)*** [63]:

$$D_l = \alpha_l \bar{v} + D_m; \quad (15)$$

in which α_l is the dispersivity of the porous medium [L]; and D_m is the molecular diffusion coefficient of the solute in the porous medium [L^2/T].

For boundary condition ***Eq. (16)***:

$$C(l,0) = 0;\ C(0,t) = C_0;\ grad(\frac{C}{C_0})(\infty,t) = 0; (l \geq 0; t \geq 0); \quad (16)$$

where C and C_0 demonstrate the radioactive, Ogata [92] solved for in Eq. (**14**) for saturated homogenous, isotropic porous medium as seen in ***Eq. (17)***, the advection-diffusion transport equation:

$$\frac{C}{C_0} = \frac{1}{2}\left[\operatorname{erfc}\left(\frac{l - \bar{v}t}{2\sqrt{D_l t}}\right) + \exp\left(\frac{\bar{v}l}{D_l}\right)\operatorname{erfc}\left(\frac{l + \bar{v}t}{2\sqrt{D_l t}}\right)\right]; \quad (17)$$

in which C_0 is the initial concentration of the tracer; and *erfc* indicates the complementary error function [93]; this equation was solved by Matlab 2017b [94,95] for longitudinal hydrodynamic dispersion data. The average flow velocity $\bar{v}$ is determined as Darcy velocity v throughout this report.

Porosity (ε) is defined by ***Eq. (18)***:

$$\varepsilon = \frac{V_C - V_S}{V_C} = \frac{PV_C}{V_C}; \quad (18)$$

in which *V* indicates the volume of the column and sand [L^3], respectively; and PV_C is the pore volume of the column [L^3].

The breakthrough curves were plotted for relative concentration $\frac{C}{C_0}$ with respect to pore volume *PV*, instead of time, for all tracer tests and simulations. Pore volume is defined as follows in ***Eq. (19)***:

$$PV = \frac{V_F}{PV_C}; \quad \textbf{(19)}$$

where V_F is the volume of fluid passed through the domain system. The Down-Tracer tests were adjusted by ***Eq. (20)*** in order to compare the curves appropriately:

$$Adjusted\ (\frac{C}{C_0}) = 1 - \frac{C}{C_0}; \quad \textbf{(20)}$$

The 95% confidence interval was calculated to present the statistical confidence level.

REV

For *nonNewtonianIcoFoam* simulation, the pressure drop ΔP was calculated by ***Eq. (21)*** to formulate to Pascal unit.

$$\Delta P = P_{output} \times \rho; \quad \textbf{(21)}$$

where P_{output} is the output pressure data; and ρ is the flow density.

Then Darcy's law ***Eq. (22)*** [96] can be used to formulate the hydraulic conductivity for this homogenous, isotropic medium domain. Comparing the data between different sphere numbers and blocks of the domain systems allows us to evaluate the REV with respect to conductivity.

$$Q = -KA\frac{dh}{dL}; \quad \textbf{(22)}$$

where Q is flow rate [L^3/T]; K is hydraulic conductivity [L/T]; A is the cross-sectional area [L^2]; and $dhdL$ represents hydraulic gradient.

The conversion between pressure drop (ΔP) to hydraulic head loss (dh) is **Eq. (23)**:

$$dh = \frac{P}{\rho g}; \tag{23}$$

where g is the gravitational acceleration [L/T^2].

Peclet number

In an advection-diffusion transport system, the Peclet number (*Pe*) [97,98] is a group of dimensionless numbers that is formulated to demonstrate the advection-diffusion transport ratio in the system. In the expression of hydrodynamic dispersion, Peclet number is defined in ***Eq. (24)*** as a comparable number across different systems.

$$Pe = \frac{vX}{D_l}; \tag{24}$$

where v is flow velocity [L/T]; and X is the mean diameter of particles [L].

Reynolds number

Darcy's law is an empirical equation, and it has been proved that Darcy's law only works on linear flow. The upper boundary of Darcy's law is identified by Reynolds number (*Re*) [63]. Reynolds number is another dimensionless number which is defined as the ratio of inertial forces and viscous forces in a fluid. We estimated Reynolds number using ***Eq. (25)*** to valid the fluid we used in experiments and simulations.

$$Re = \frac{\rho v L}{\mu}; \tag{25}$$

where, ρ is the density of the fluid [M/L^3]; μ is the dynamic viscosity of the fluid; v is the velocity of the fluid; and L is the length of the system.

Chapter 4. Results and Discussion

Column experiments

The basic data for column, sand, and fluid were collected at room temperature during the beginning of the experiments and listed in ***Table 1.*** The subscripts *C* and *S* represent the variable for column and sand, respectively.

Table 1. Column and Sand Data

Column		Sand		Fluid	
Length (L_C)	86.5 cm	Density(ρ_S)	2.65 g/cm^3	DIW Density (ρ_{DI})	998.0 kg/m^3
Radius of Column (r_C)	1.25 cm	Mass(m_S)	736.81 g	0.3% GG Density (ρ_3)	999.45 kg/m^3
Volume of Column (V_C)	424.61 cm^3	Volume of Sand (V_S)	278.04 cm^3	0.5% GG Density (ρ_5)	999.95 kg/m^3
Pore Volume (PV_C)	146.57 cm^3	Mean Radius of Sand (r_S)	3.77E-04 m	Flow rate (Q_C)	40 mL/hr
Porosity(ε_C)	0.3452	Mean Diameter of Sand (X_S)	7.54E-04 m	Darcy's Velocity (v_C)	2.26E-05 m/s

Breakthrough Curve

The breakthrough curves of DIW tracer tests for relative concentration of radioactivity of the samples with respect to number of pore volume are presented in ***Figure 3***. All the breakthrough curves were corrected with time to meet at the middle point of curves; this means that when PV=1, the relative concentration should be 0.5, according to conservation equation.

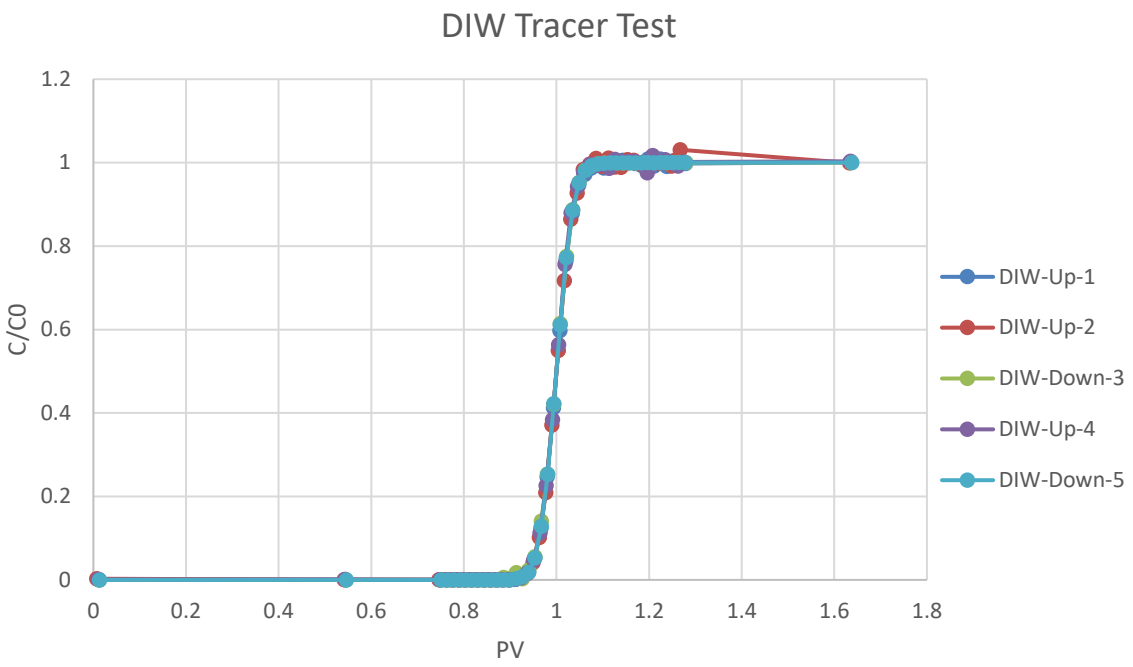

Figure 3. DIW Tracer Tests Breakthrough Curve

The 95% confidence interval (CI) was calculated and plotted in ***Figure 4***.

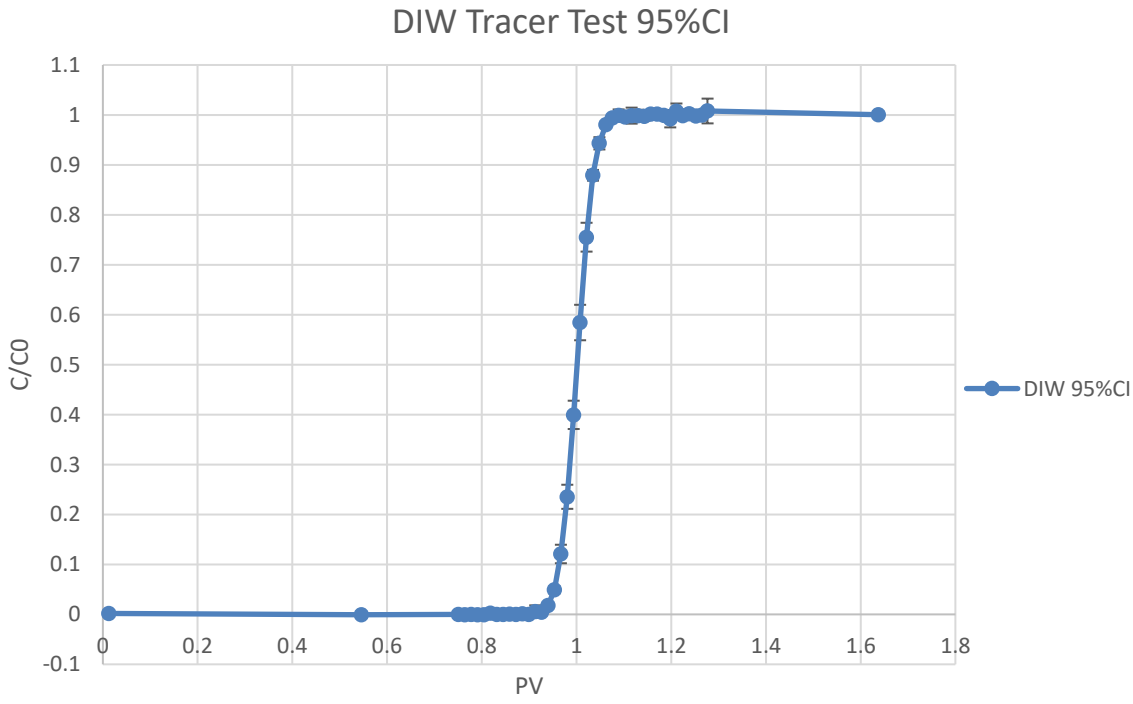

Figure 4. DIW Tracer Tests 95% Confidence Interval Breakthrough Curve

From the breakthrough curves of DIW tracer tests, it is clear that the hydrodynamic dispersion for DIW is very stable and consistent for all five DIW tracer tests. For 0.3% and 0.5% guar gum tracer tests, (abbreviated to 3GG and 5GG respectively), the breakthrough curve and 95% CI were calculated and plotted in ***Figure 5*** to ***Figure 8***.

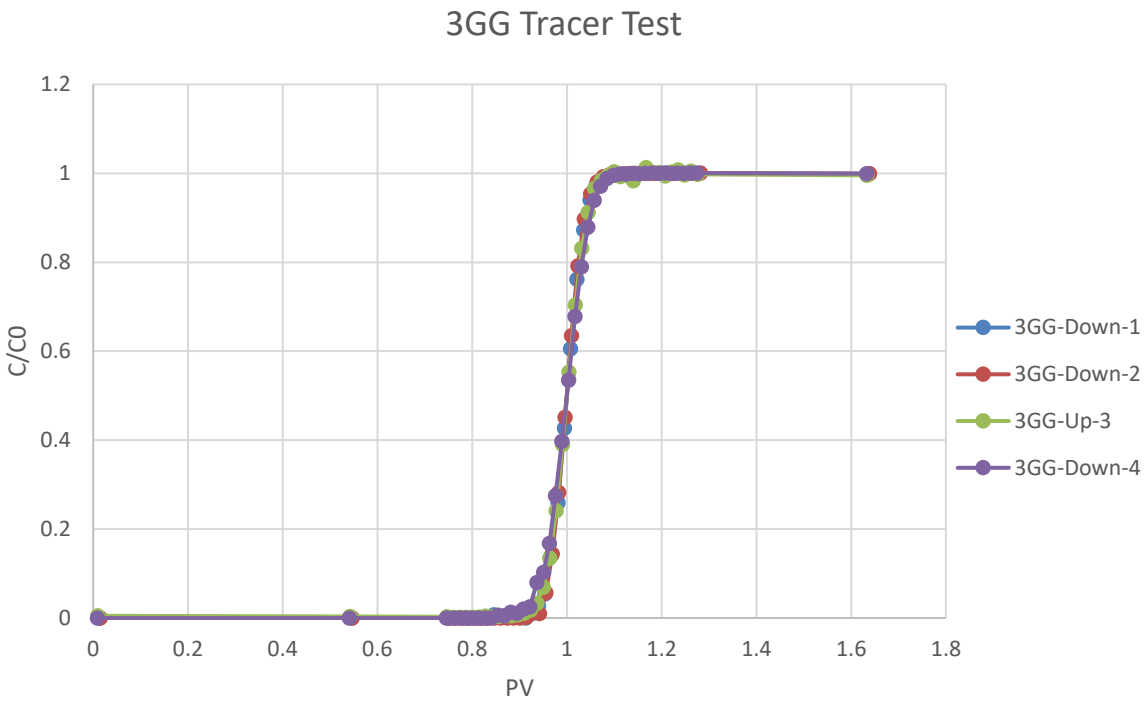

Figure 5. 0.3% Guar Gum Tracer Tests Breakthrough Curve

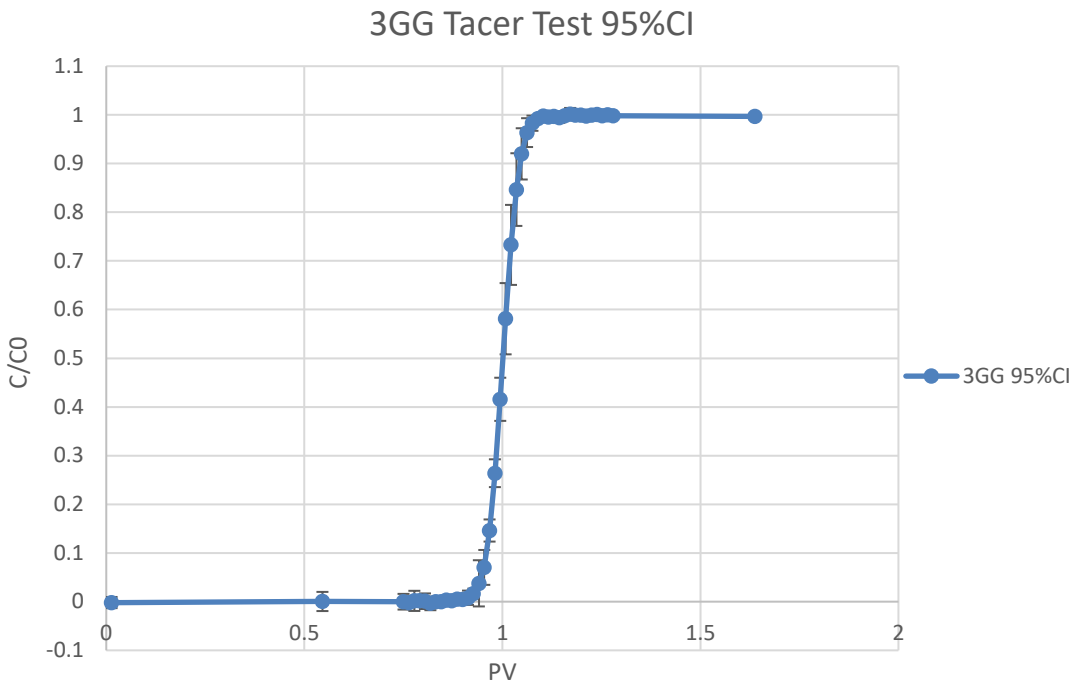

Figure 6. 0.3% Guar Gum Tracer Test 95%CI

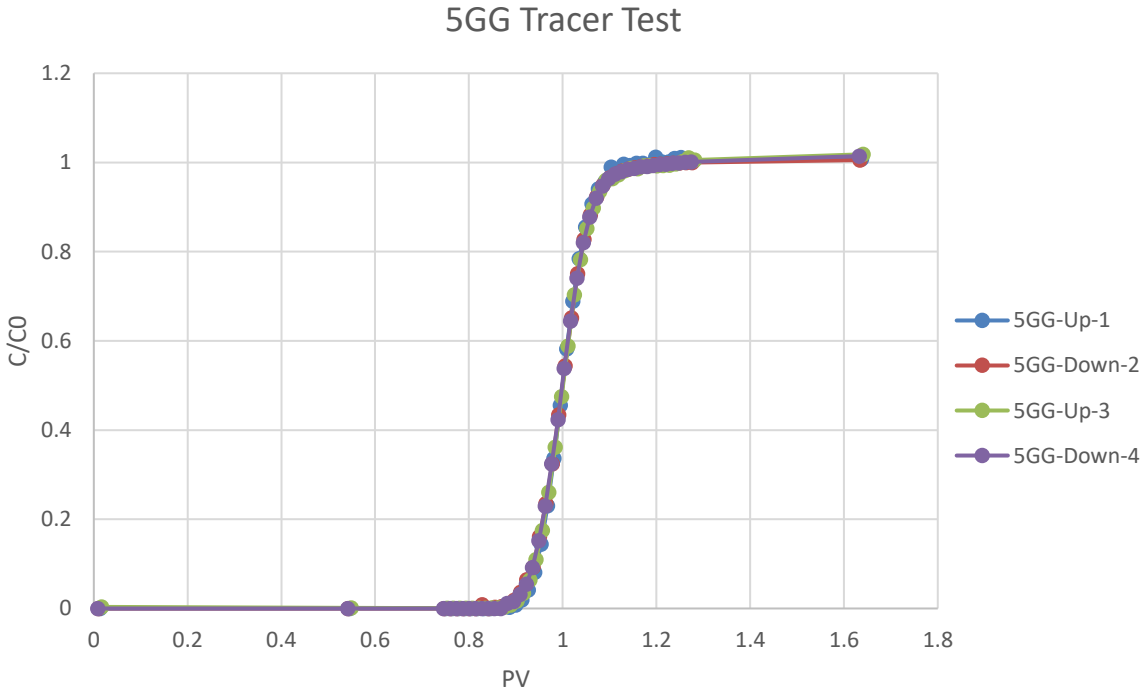

Figure 7. 0.5% Guar Gum Breakthrough Curve

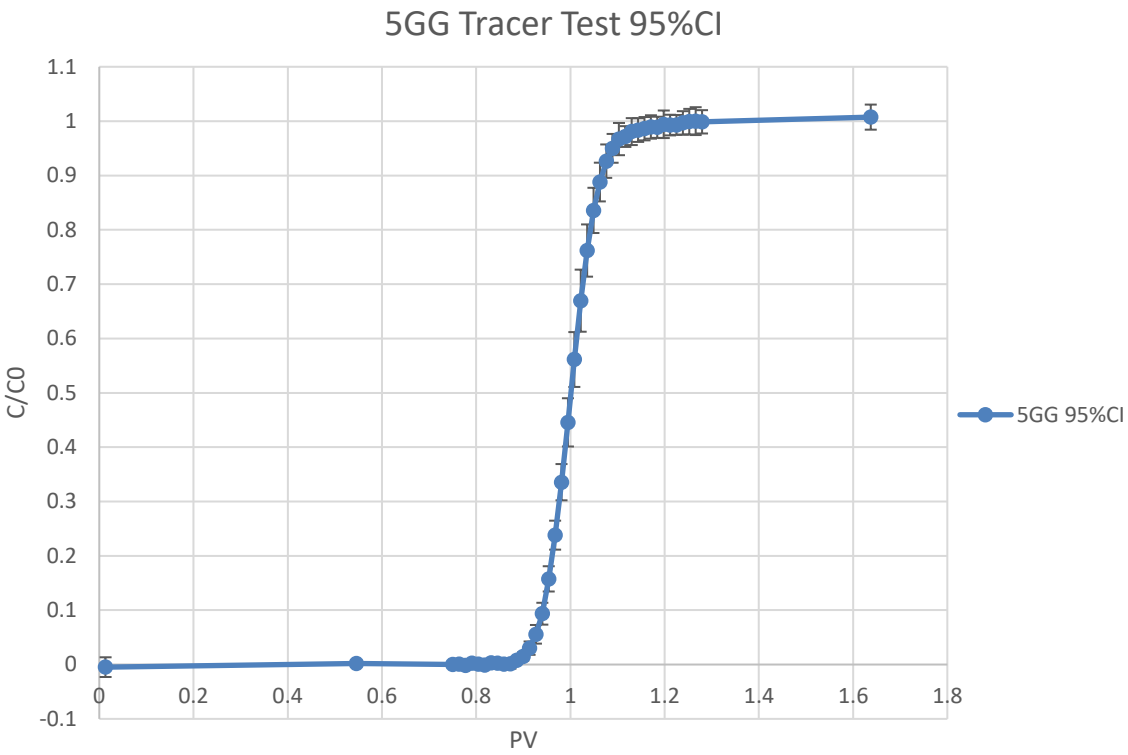

Figure 8. 0.5% Guar Gum Tracer Test 95% CI

The post-DIW tracer tests breakthrough curve and the 95% CI are presented in ***Figure 9*** and ***Figure 10***.

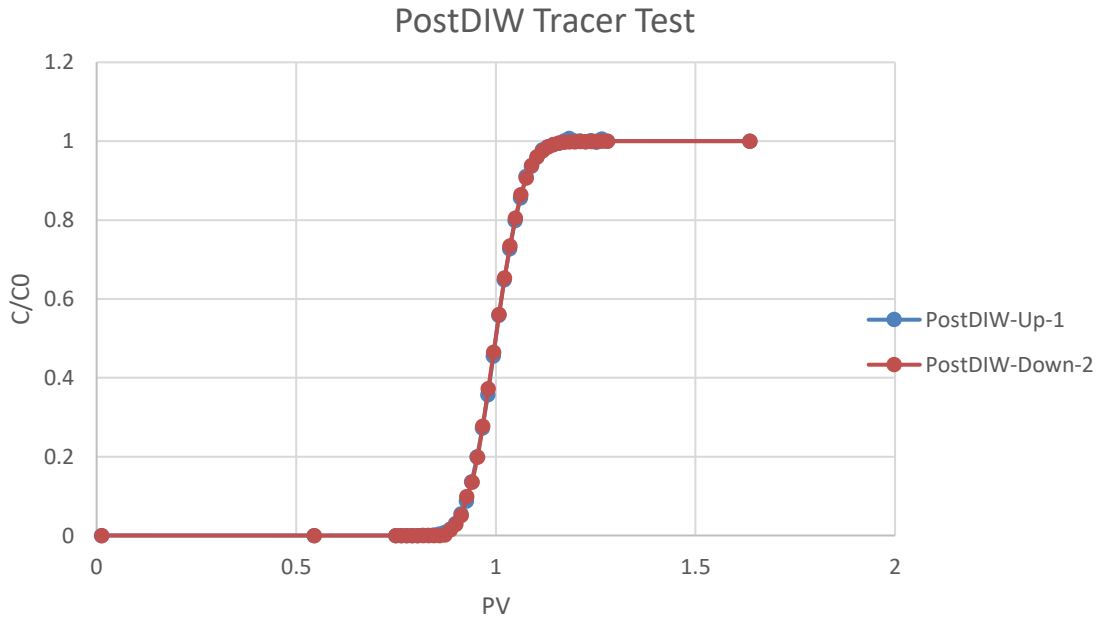

***Figure 9. Post*-DIW Tracer Test Breakthrough Curve**

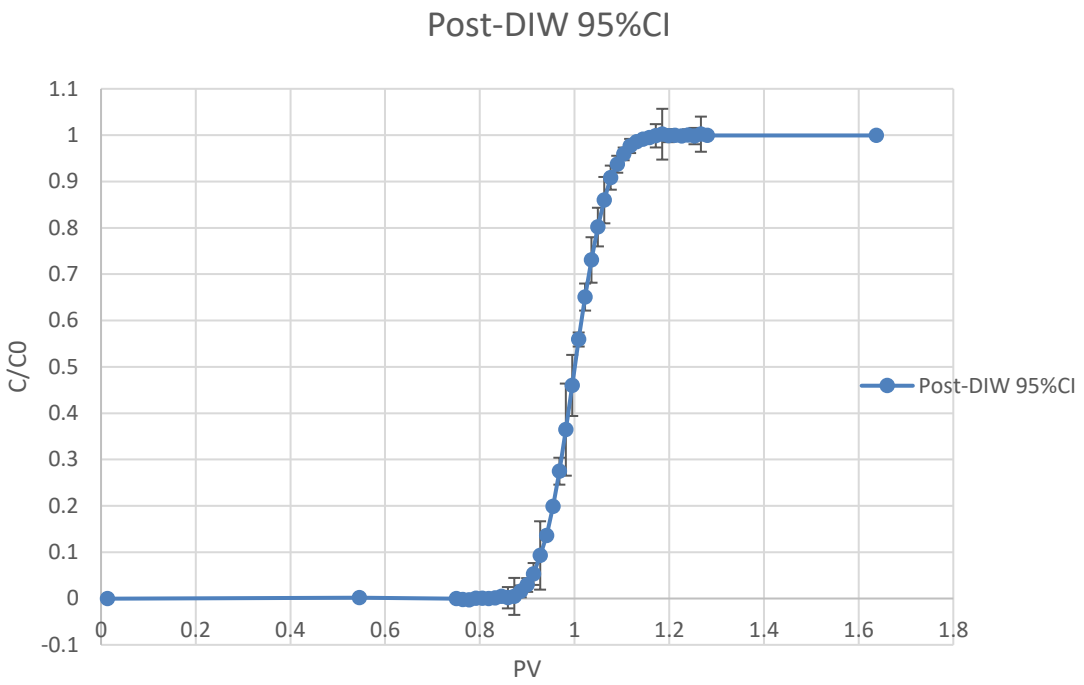

Figure 10. Post-DIW Tracer Test Breakthrough Curve 95% CI

As can be observed from the 95% CI curves, experimental results from both 0.3% and 0.5% guar gum solutions vary relatively larger than DIW, but we cannot obtain much information about dispersion from the separate breakthrough curve. When we compared the mean value of the breakthrough curve calculated from each time point samples, the difference between different fluids is clearer. ***Figure 11*** shows that from DIW to 0.3% guar gum solution, 0.5% guar gum solution, and eventually post-DIW, the curves vary from sharp to smooth. Between DIW and 0.3% guar gum solution, the trend is not obvious, but from DIW to 0.5% guar gum solution, the curves change clearly, and the first species took less time to get to the outlet flow. It looks like the hydrodynamic dispersion is becoming larger in guar gum solution than DIW, but the post-DIW shows an unusual trend that doesn't follow this pattern.

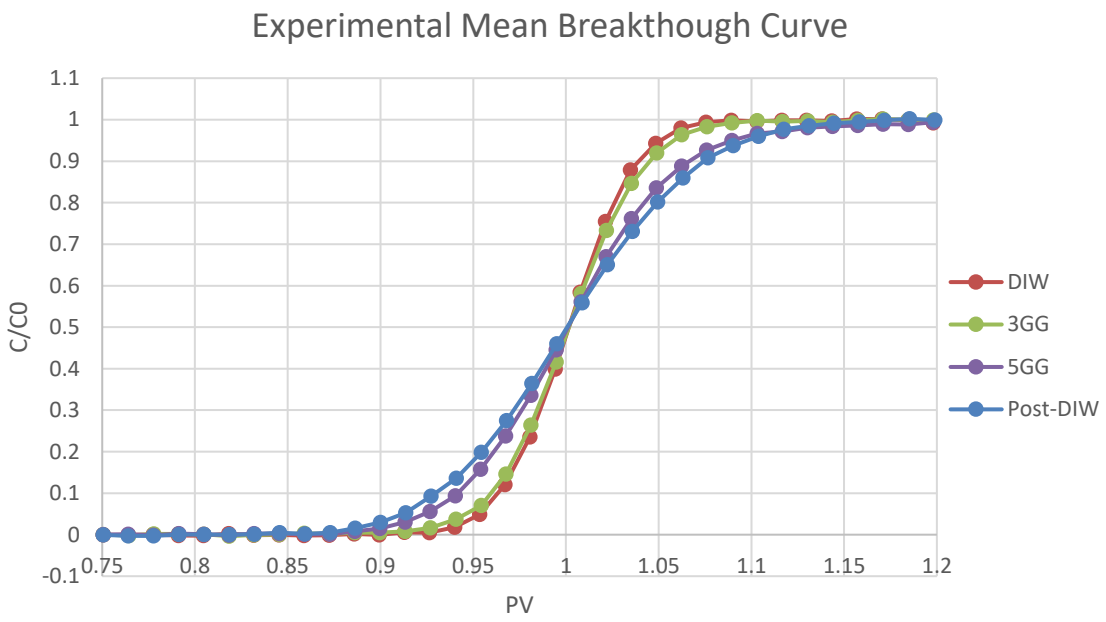

Figure 11. Experimental Mean Breakthrough curve comparison

With regard to the abnormal post-DIW tracer test results, the possible reason could be: 1) although we pumped 10 times the pore volume of DIW to flush the column after the guar gum tracer tests and before the post-DIW tracer tests, there was not a way to make sure the guar gum solution had been pushed out of the column completely; 2) the potential residue might cause multiple-phase transport and lead to unstable advection-transport between DIW and guar gum solution; 3) guar gum solution might have occupied some pores or pore connections and turned the uniform medium to variable media, which means that part of the fluid moved faster than other parts, and the dispersion became greater.

Hydrodynamic Dispersion

After calculated the hydrodynamic dispersion based on advection-diffusion transport ***Eq. (17)*** through MatLab, the overall dispersion data comparison was plotted as ***Figure***

12. The breakthrough curves were corrected with time in MatLab to obtain the dispersion results.

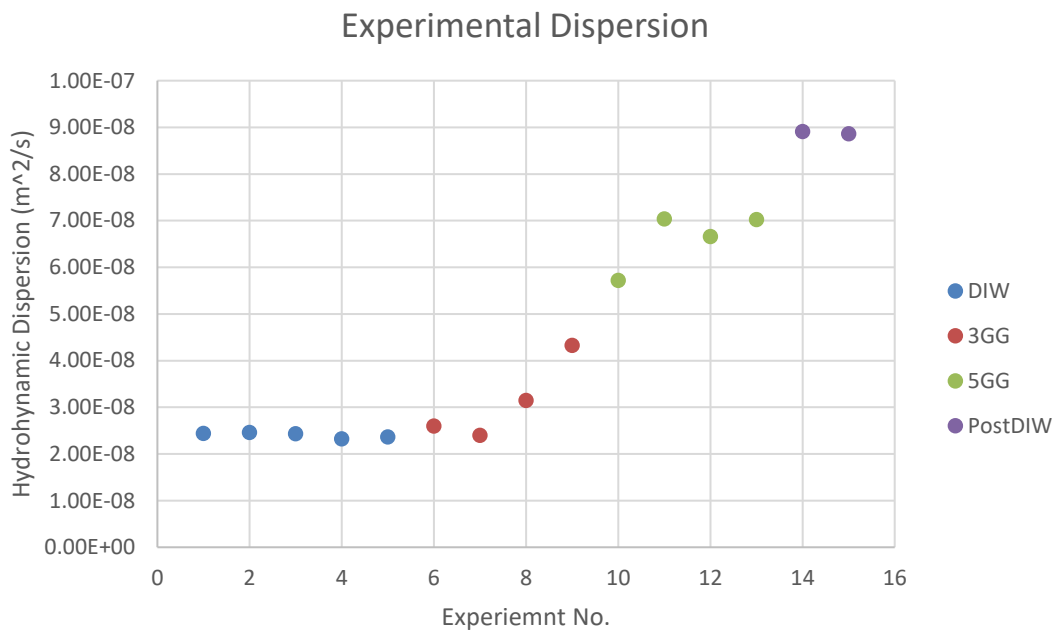

Figure 12. Experimental Hydrodynamic Dispersion Comparison

The comparison data indicates an explicit trend in which hydrodynamic dispersion increases as the fluid goes from Newtonian fluid to non-Newtonian fluid, and increases with the concentration increase of guar gum solution.

The mean dispersion data variation in ***Figure 13*** matches the dispersion increasing trend with the fluid changes from Newtonian fluid to non-Newtonian fluid, except for the post-DIW tracer tests. The 95% interval is very small in DIW tracer tests, but varies in a relative larger interval in non-Newtonian fluids. This phenomenon reflects the difficulty of investigating properties of non-Newtonian fluids and the instability of non-Newtonian fluids.

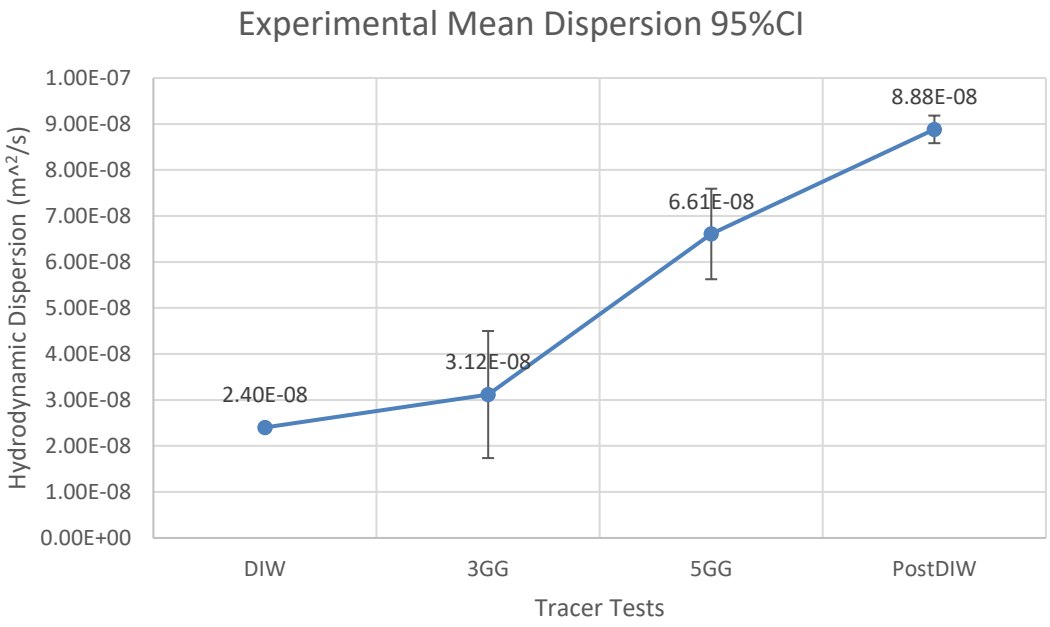

Figure 13. Experimental Mean Dispersion 95% CI

Although the dispersion data fluctuated for both 0.3% and 0.5% guar gum solution, there seems to be a trend that with tracer tests conducted more, the dispersion increased. However, the breakthrough curves in every solution show overlaps between each of the tracer tests.

Advection-Diffusion Model Fitting

The experimental dispersion was fitted with advection-diffusion transport function ***Eq. (17)***, or the analytical hydrodynamic dispersion model, to evaluate our data and presented it in ***Figure 14***. Only one example was selected from each fluid.

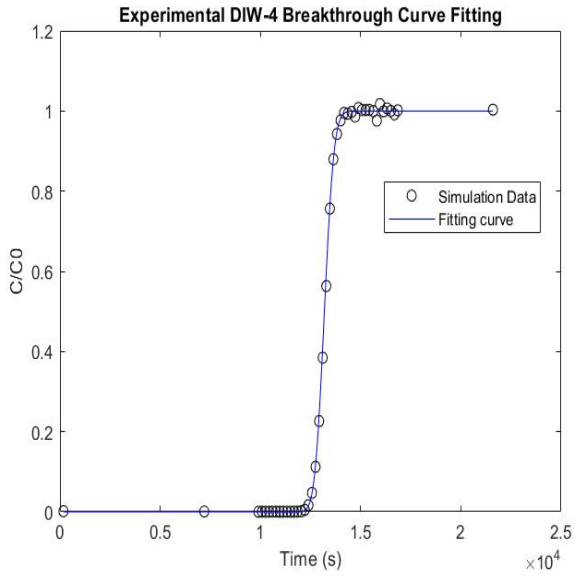

(a) DIW Fitting;

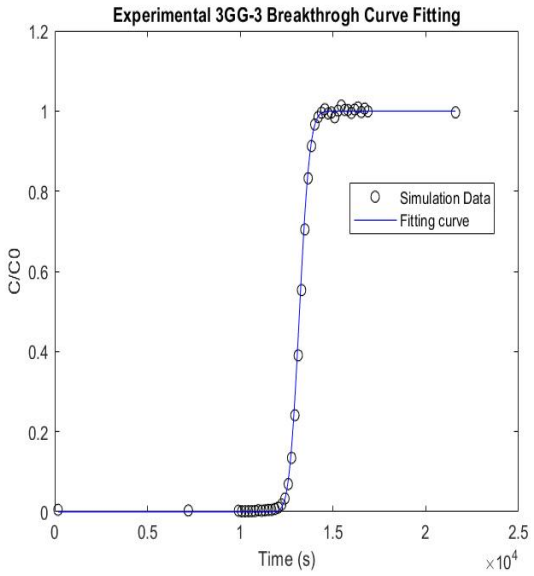

(b) 0.3% Guar Gum Fitting;

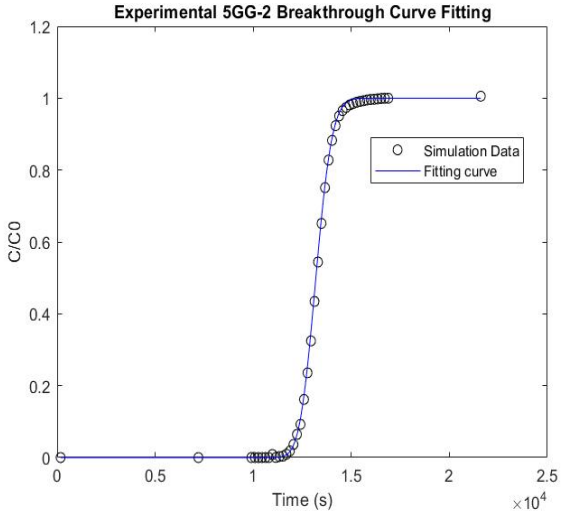

(c) 0.5% Guar Gum Fitting;

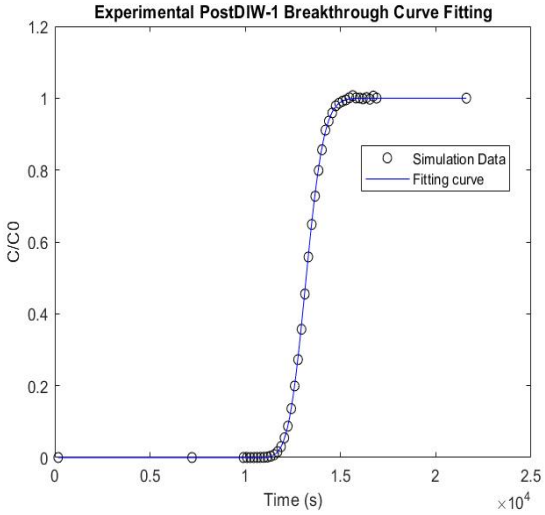

(d) Post-DIW Fitting;

Figure 14. Experimental Breakthrough Curve Fitting

In the fitting graph, the sample spots fit the model curve very well for the four types of tracer tests. In terms of dispersion sensitivity, we picked the mean hydrodynamic dispersion of the 0.3% guar gum solution ($D_l = 3.12E-8\ m^2/s$), divided by two, or multiplied by two, to show the model curve variations in ***Figure 15***.

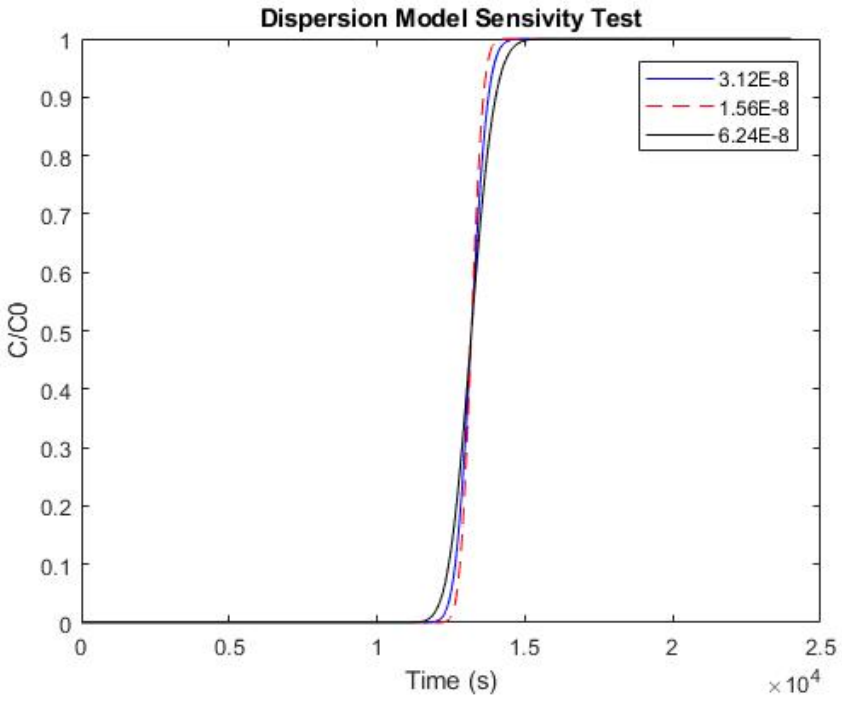

Figure 15. Analytical Hydrodynamic Dispersion Model Sensitivity

The analytical hydrodynamic dispersion model sensitivity shows that even with the hydrodynamic dispersion doubled or cut in half, the curve fluctuated in a fairly small range. It indicates that although the experimental results for 0.3% and 0.5% guar gum solutions varied during different tracer tests, it is still within experimental error. Since the tracer tests had good repeatability, the experimental results can be considered reliable.

Peclet Number

We calculated the Pe number in the expression of hydrodynamic dispersion in ***Figure 16***.

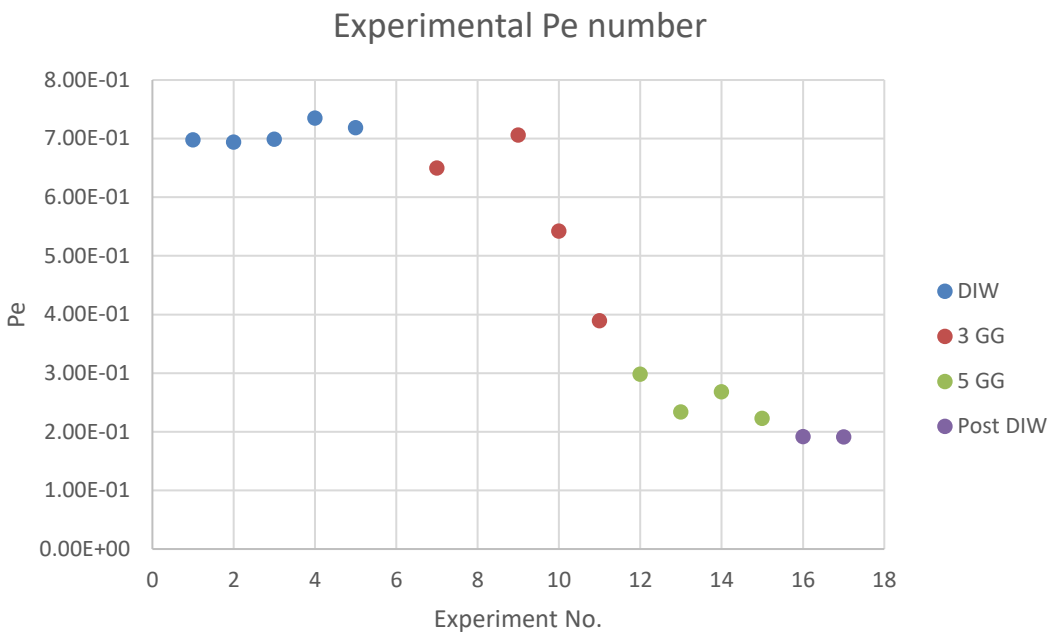

Figure 16. Experimental Pe Number

Reynolds number

Reynolds numbers were calculated and presented in ***Table 2*** based on dynamic viscosity at zero shear rate and at infinite shear rate.

Table 2. Experiment Reynolds Number

	Re_0	Re_{Inf}
DIW	20.14477896	
3GG	0.143888426	6.437113816
5GG	0.014396041	5.914989667

Re_0 is the Reynolds number at zero shear rate; Re_{Inf} is the Reynolds number at infinite shear rate.

Simulation

Sphere Packing

The packed data for different domain systems is presented in ***Table 3***.

Table 3. Packed Domain Systems Data

N_S	Length (L_0) (m)	Porosity (ε_0)	Log mean (μ_{log})	Variance (σ^2)
1000	0.00710809	0.370311	-7.89035	0.00431891
2000	0.00895564	0.366478	-7.88425	0.00431891
3000	0.0102516	0.369881	-7.88705	0.00431891
4000	0.0112894	0.369882	-7.88525	0.00431891
5000	0.0121547	0.368456	-7.88635	0.00431891

The picture of the actual domain with two reservoirs generated from *paraView* are shown in ***Figure 17***.

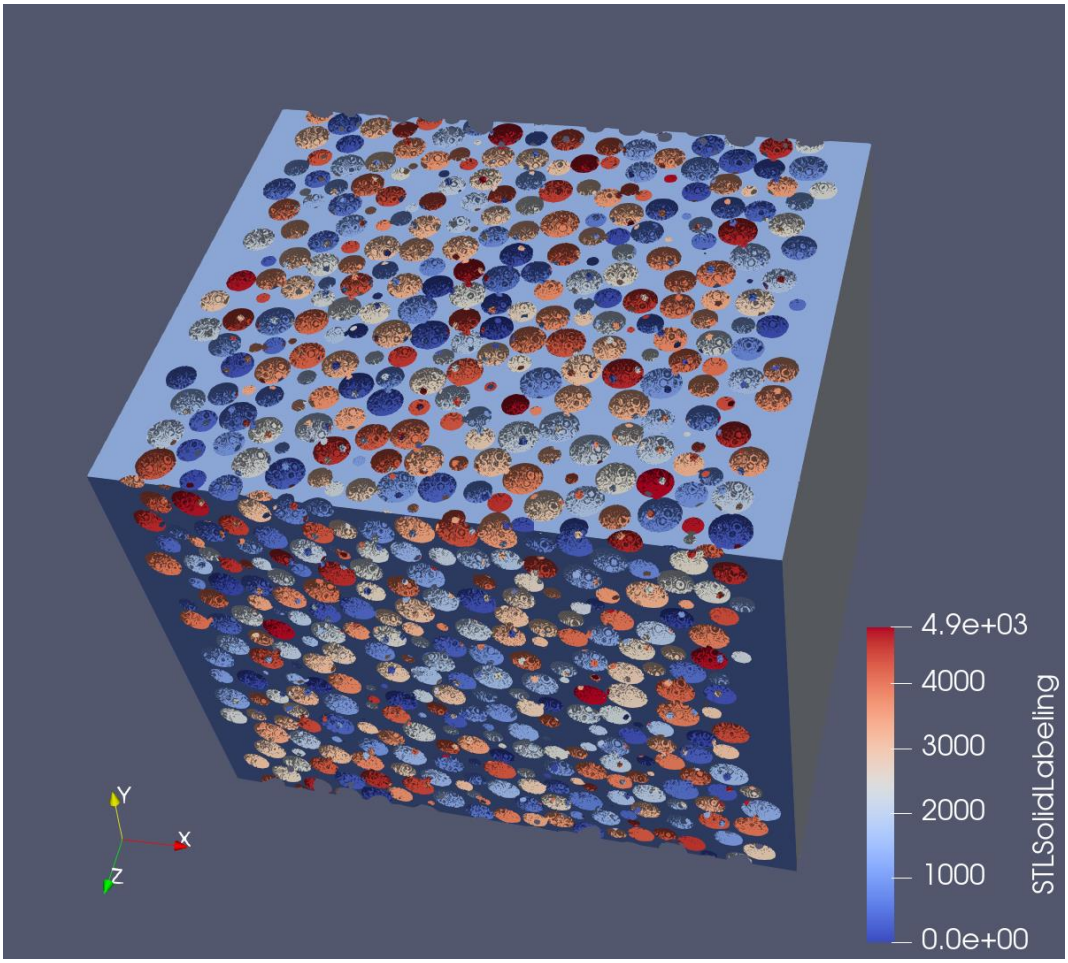

Figure 17. Picture of the Domain from ParaView

Pressure Drop

For each sphere numbers of domains (1000, 2000, 3000, 4000, 5000), with different blocks (100^3, 200^3, 300^3, 400^3, 500^3), for 0.3% guar gum solution at $v = 0.00005\ m/s$. The rheological measurements for the viscosity of DIW and guar gum solutions are listed in *Table 4*.

Table 4. Rheological Cross-Model Parameters for Guar Gum Solutions

	μ_0 (Pa s)	μ_{Inf} (Pa s)	*m*	*n*
DIW	0.000970		0	
0.3% Guar Gum	0.136	0.00304	0.0455	0.683
0.5% Guar Gum	1.36	0.00331	0.322	0.707

μ_0: dynamic viscosity at zero shear rate; μ_{Inf}: dynamic viscosity at infinite shear rate; *m* and *n*: fitting parameters.

The pressure drop data was collected from *nonNewtonianIcoFoam*, converted it to Pascal, and plotted in ***Figure 18***. From the individual sub-figures, pressure drop decreases as blocks number grows. All of the sphere domains that have blocks between 100^3, 200^3, and 300^3 came to steady-state in less than 0.1s. However, when the blocks reached 400^3 and 500^3, we started to see instability of the system. It might take longer for the systems with blocks greater than 300^3 to get to steady-state. Under limited research time, we couldn't get a steady-state for domain system: N_S = 4000 with 400^3 and 500^3 blocks, and N_S = 5000 with 500^3 blocks.

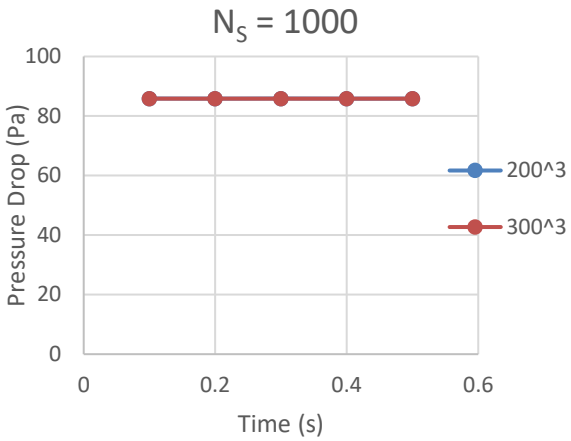

(a) N_S = 1000;

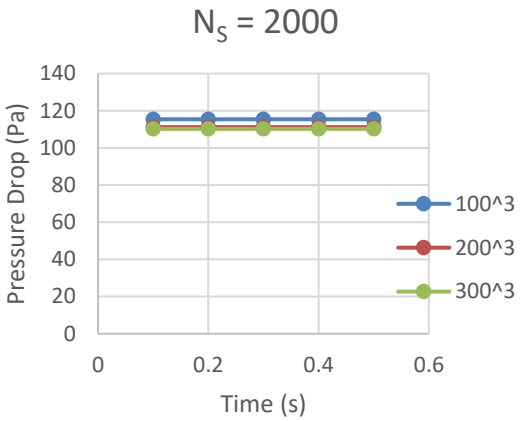

(b) N_S = 2000;

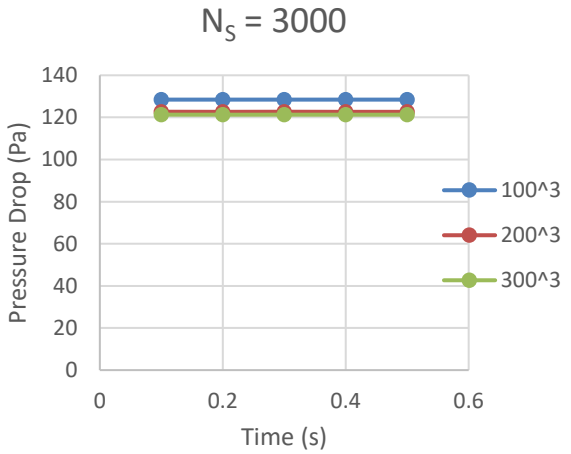

(c) N_S = 3000;

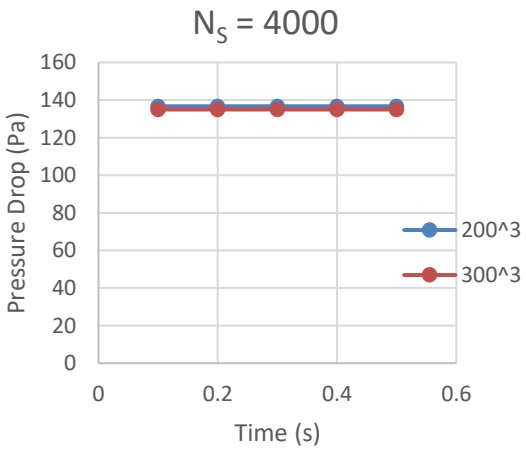

(d) N_S = 4000 (1)

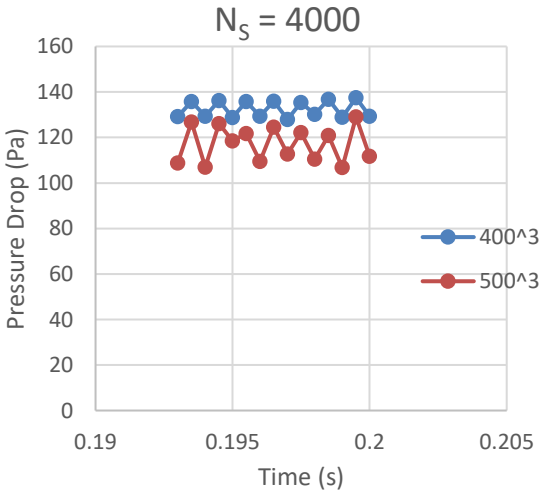

(e) N_S = 4000 (2);

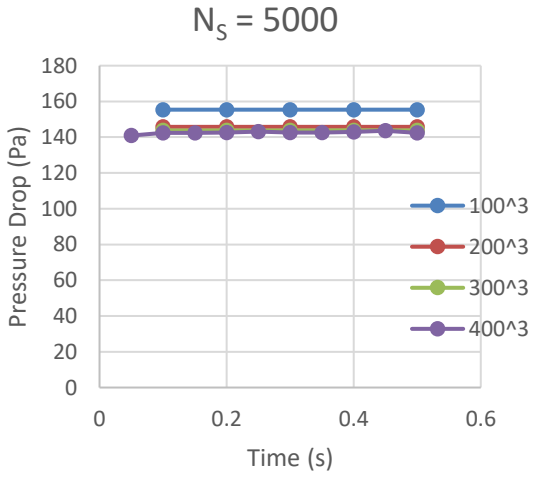

(f) N_S = 5000 (1);

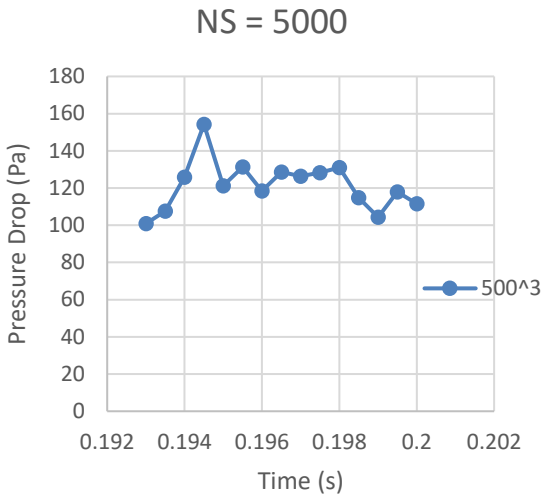

(g) N_S = 5000 (2);

Figure 18. Pressure Drop Varies with Different Spheres and Blocks

In order to present the pressure drop variation more explicitly, the average pressure drop and average pressure drop per length was calculated for each simulation and depicted the result in ***Figure 19*** and ***Figure 20***.

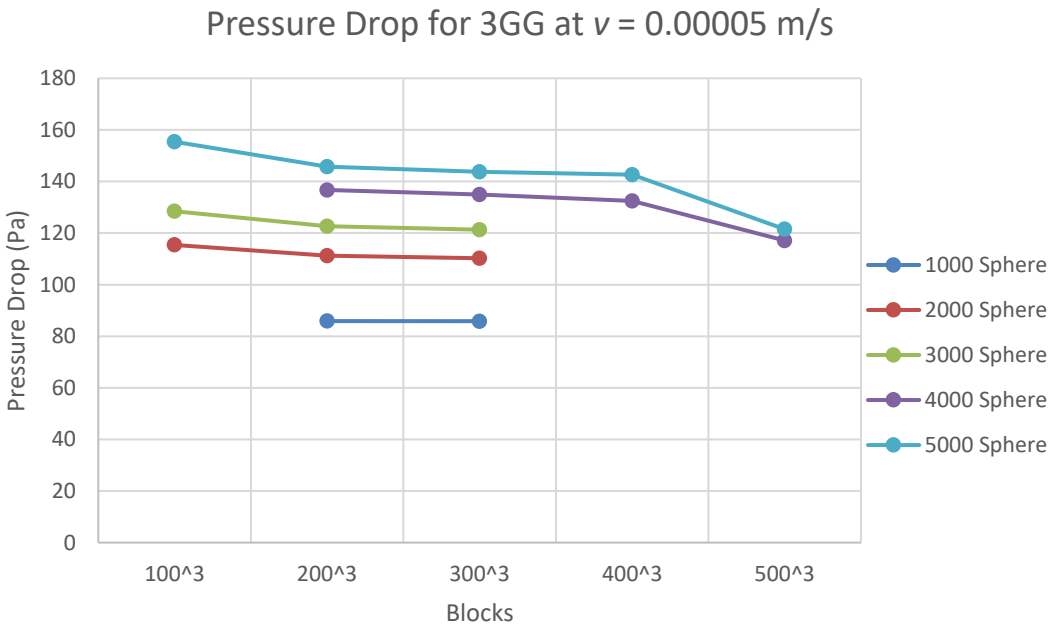

Figure 19. Pressure Drop for 0.3% Guar Gum at v = 0.00005 m/s

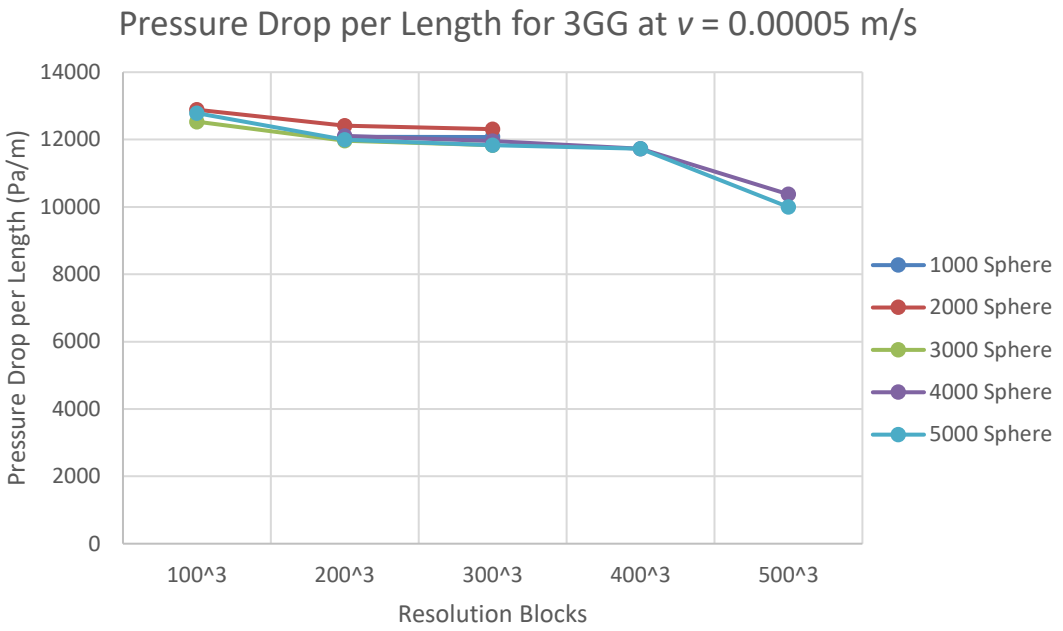

Figure 20. Average Pressure Drop per Length for 0.3% Guar Gum at v = 0.00005 m/s

From this average pressure drop and average pressure drop per length comparison graph, a similar pattern appeared repeatedly. In each sphere system, from 100^3 to 200^3, the average pressure drop had a clear decline; from 200^3 to 300^3, the average pressure drop stayed relative stable; from 300^3 to 400^3, although the average pressure drop variation was small, the system encountered unstable pressure through the same simulation time interval; and at 400^3 to 500^3, the average data were based on unstable pressure drop, therefore it will not be used for analysis. We eliminated the domain systems for which we could not obtain steady-state, considered the constraints of our scientific computing resources, and optimized the accuracy of the simulation. Eventually, the domain system with 4000 spheres and 300^3 blocks was selected as the domain system applied for scalarTransport.

REV

Hydraulic conductivity was calculated using Darcy's law. The relationship between hydraulic conductivity and sphere numbers is presented in ***Figure 21***. The REV graph confirmed our decision for the selected domain. Because the refinement level of the systems was 2, the resolution level required to reach REV was significantly reduced.

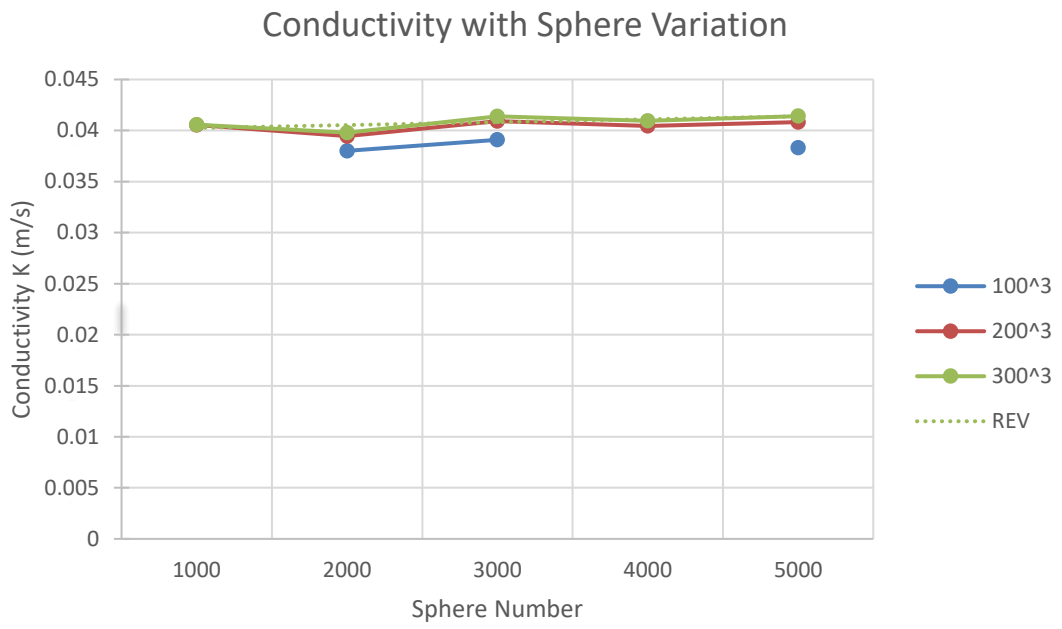

Figure 21. REV With Respect to Conductivity Under Different Domain Systems

ScalarTransport

The domain with 4000 Spheres and 300^3 blocks was selected based on the analysis above to conduct *scalarTransportFoam* for three fluids: DIW, 0.3% guar gum, and 0.5% guar gum solutions; at three velocities: 0.0005m/s, 0.00005m/s, and 0.000005m/s; and two molecular diffusion coefficients: 0 and 2.05E-10. The relative concentrations of the species were collected at the outlet flow, and we plotted breakthrough curves and calculated dispersion based on the same hydrodynamic dispersion model we used for experimental tracer tests. Because the simulations are computationally expensive and require large storage space and computing resources, we were unable to

complete all the simulations in Dogwood. ***Figure 22*** to ***Figure 24*** show the breakthrough curves with different velocity for simulation results.

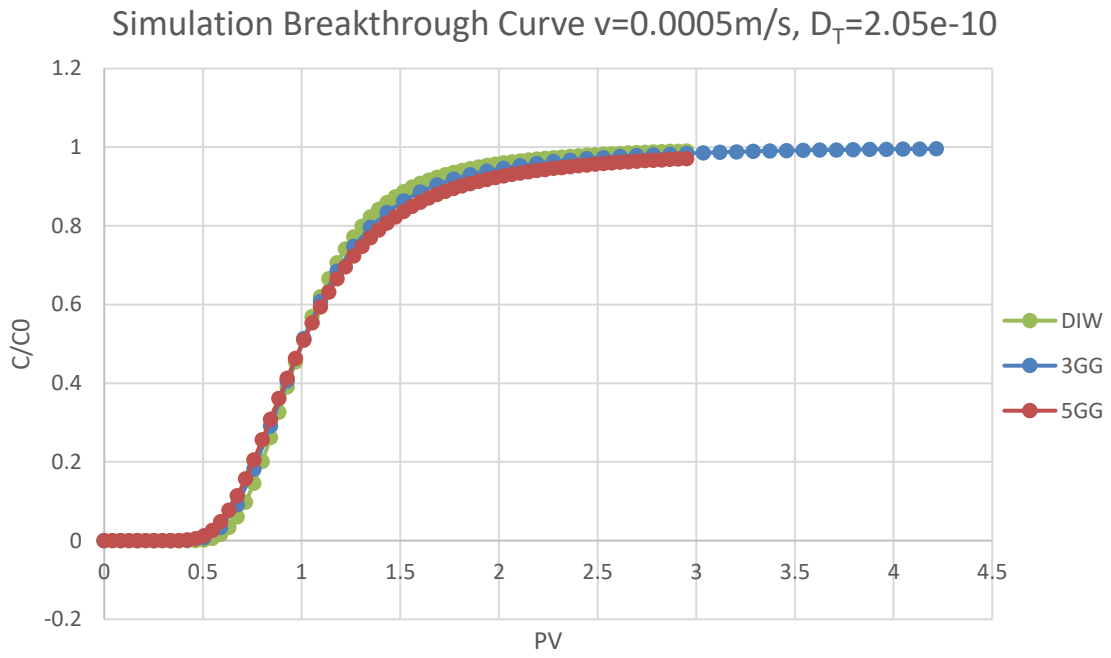

Figure 22. Simulation Breakthrough Curve at v=0.0005m/s, D_T=2.05E-10

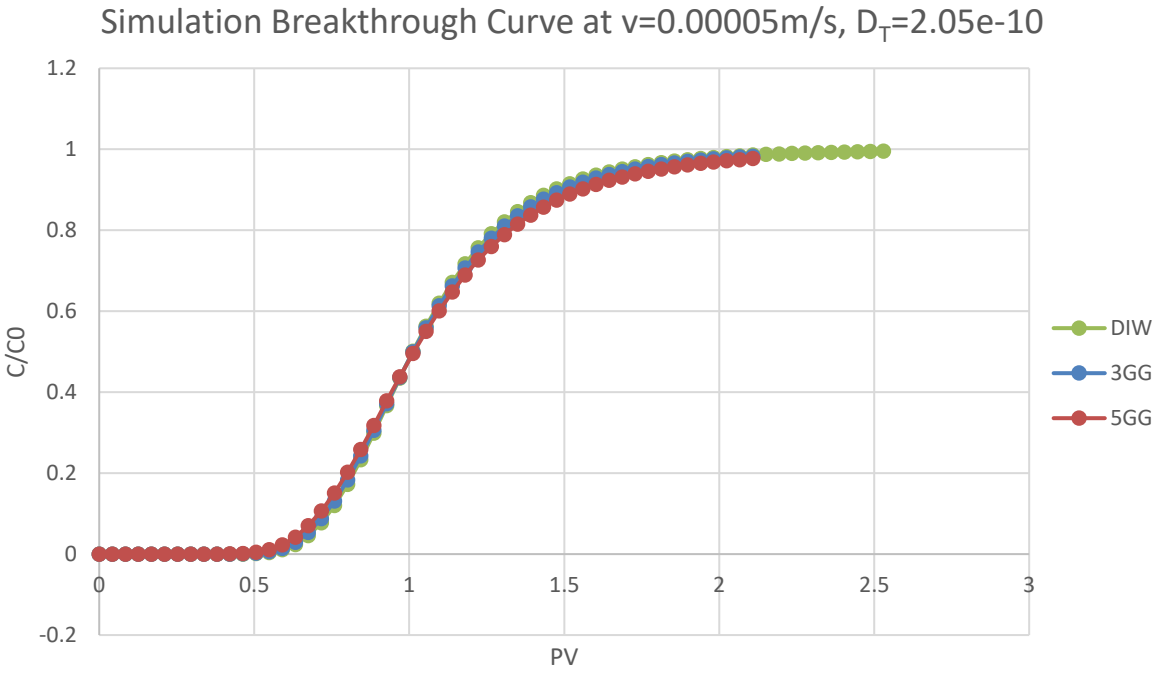

Figure 23. Simulation Breakthrough Curve at v=0.00005m/s, D_T=2.05E-10

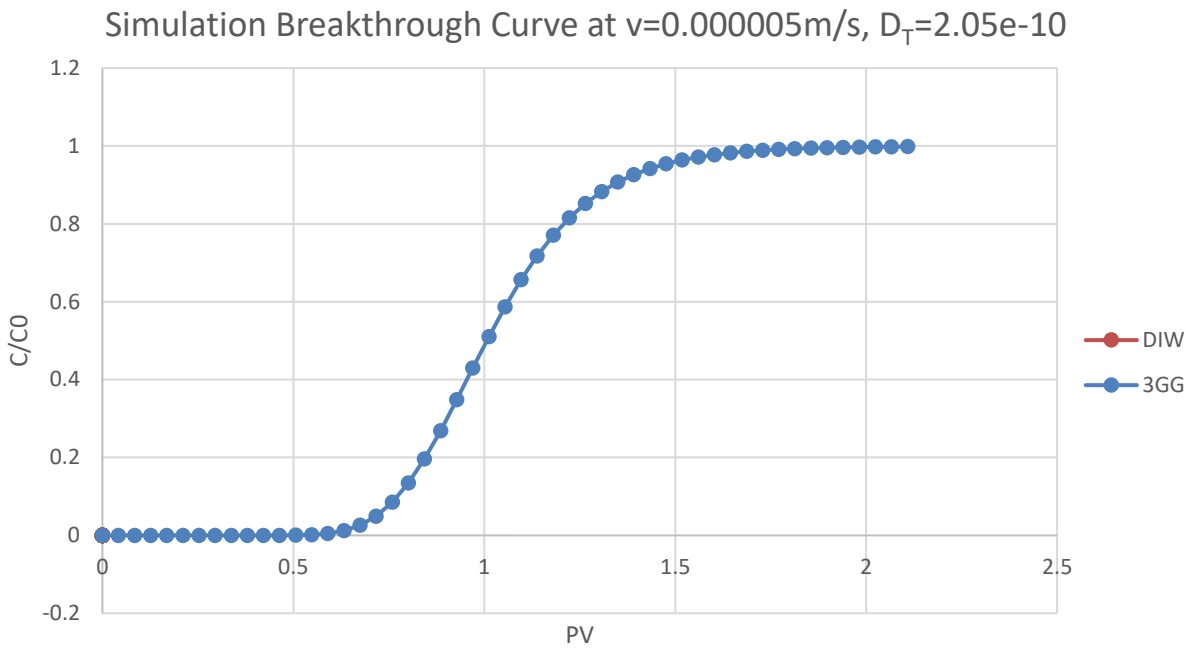

Figure 24. Simulation Breakthrough Curve v=0.000005m/s, D_T=2.05E-10

In the breakthrough curve in each different velocity, when v=0.0005m/s and v=0.00005m/s, the same sharp to smooth trend showed up as observed in the experimental breakthrough curve. From the top curve to the bottom curve is from DIW to 0.3% guar gum to 0.5% guar gum solutions. The shape of the curve varies more between different fluids when v=0.0005m/s, the curves are close to each other when v=0.00005m/s; and the breakthrough curve of DIW and 0.3% guar gum nearly overlap with each other when v=0.000005m/s.

We conducted some comparison simulations with D_T=0 to observe the impacts of the variations of D_T, and the according breakthrough curve are presented in ***Figure 25*** to ***Figure 27***.

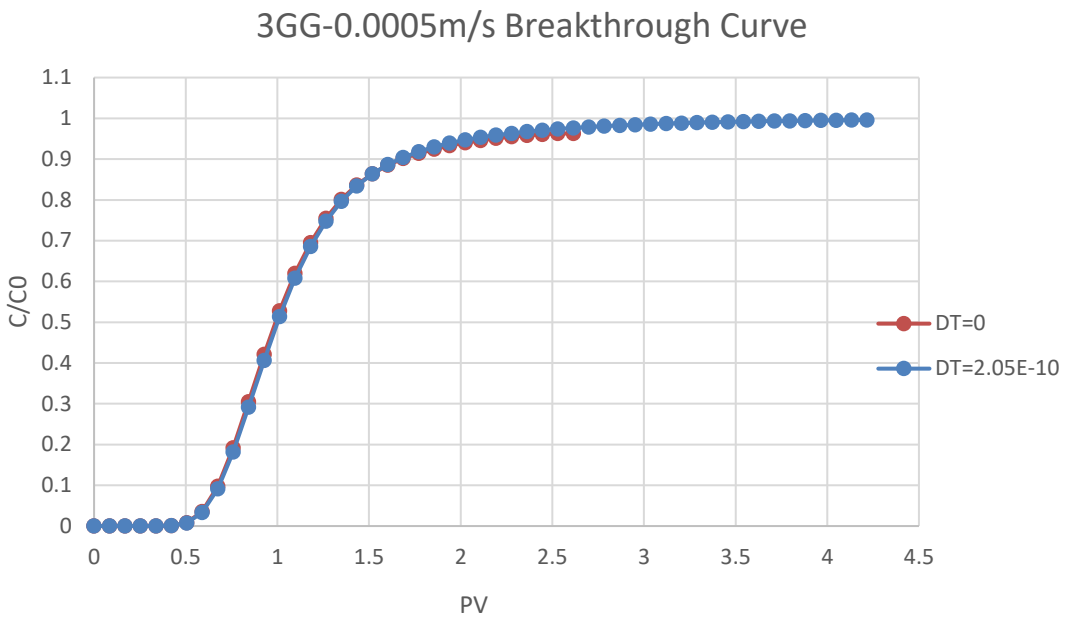

Figure 25. Simulation 0.3% Guar Gum at v=0.0005m/s Breakthrough Curve

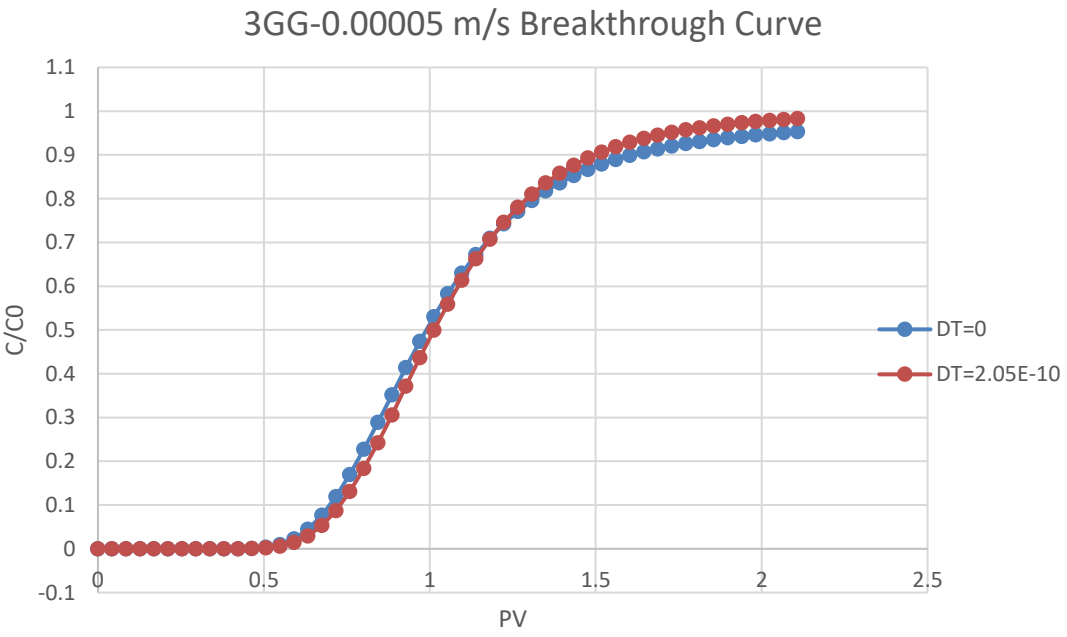

Figure 26. Simulation 0.3% Guar Gum at v=0.000005m/s Breakthrough Curve

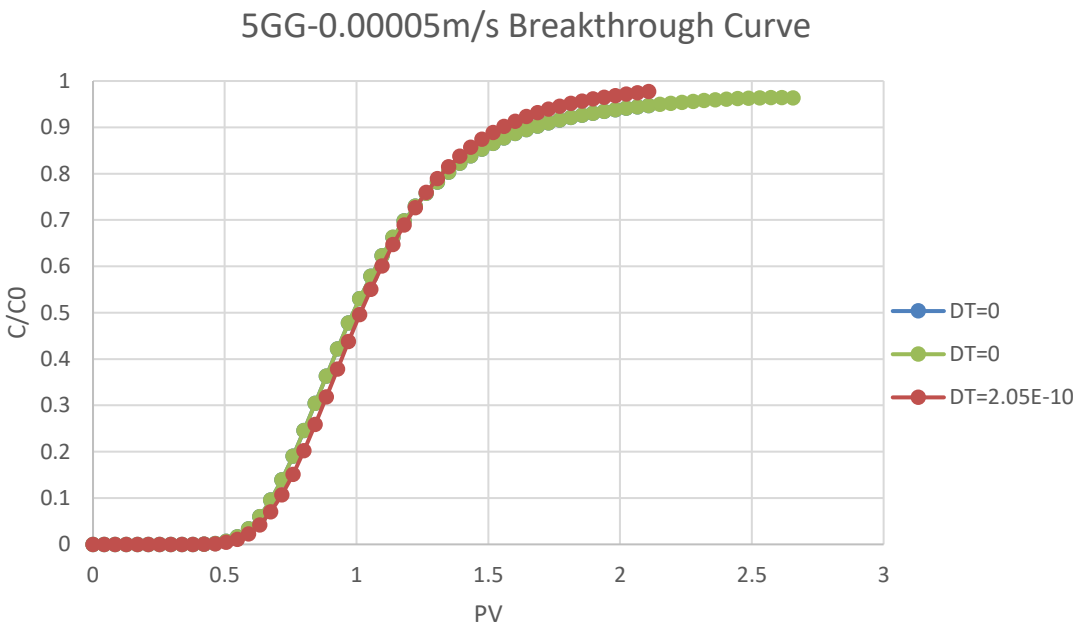

Figure 27. Simulation 0.5% Guar Gum at v=0.00005m/s Breakthrough Curve

For the breakthrough curve with different D_T, the D_T=0 curves are slightly smoother than D_T=2.05E-10 in all compared groups. In different velocity groups, the change of curve shape between two D_T values is smaller at v=0.0005m/s than v=0.00005m/s, meaning that when velocity is larger, the effects of molecular diffusion are relatively insignificant. This agrees with the molecular diffusion pattern that molecular diffusion is negligible when velocity is large.

However, all the curves took much longer to reach the relative concentration equal to one. The breakthrough curves do not appear to match the experimental results. We calculated the hydrodynamic dispersion data to get more information. ***Figure 28*** and ***Figure 29*** plot the simulation hydrodynamic dispersion data comparison between DIW, 0.3% guar gum and 0.5% guar gum solutions at different velocities and different D_T values. For velocity decreases from 0.0005m/s to 0.000005m/s, the dispersion in each fluid decreases by the same order accordingly. For each velocity group, the

hydrodynamic dispersion decreases from 0.5% guar gum, to 0.3% guar gum, to DIW, which is the same trend as the experimental data shows. The variation of hydrodynamic dispersion data these three fluids is larger when the velocity is higher; at v=0.0005m/s, the difference of hydrodynamic dispersion is clear between these three fluids; but at v=0.000005m/s, the hydrodynamic dispersion varies in a very small range between DIW and 0.3% guar gum fluids. For 0.3% guar gum and 0.5% guar gum solutions, at velocity equal to 0.00005m/s, (which is roughly the experimental tracer test velocity), the hydrodynamic dispersion of 0.5% guar gum solution is slightly larger than that of 0.3% guar gum, but the difference between them is not as large as what we found in the experimental results.

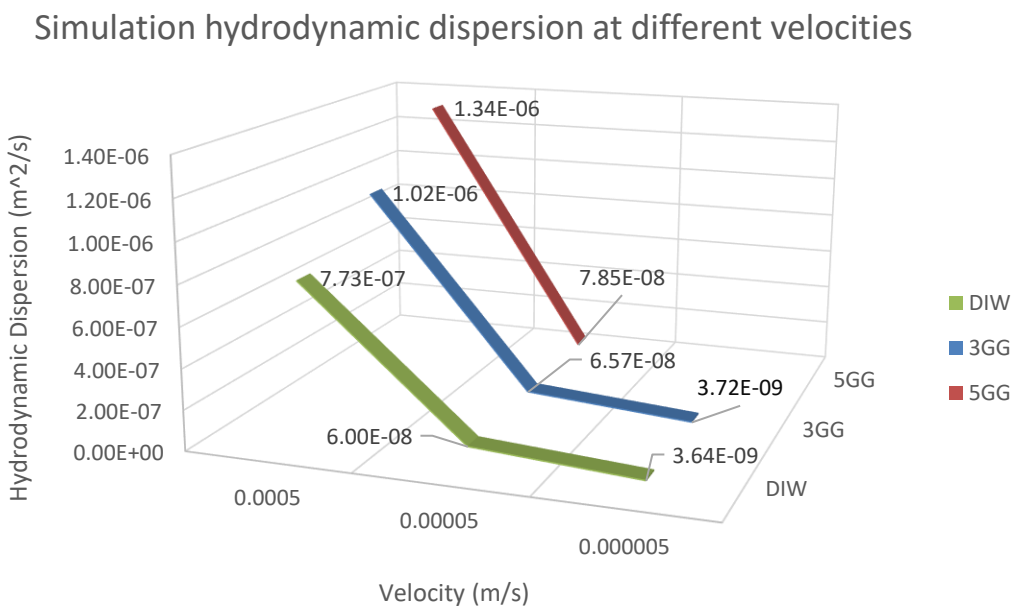

Figure 28. Simulation Hydrodynamic Dispersion at different velocities

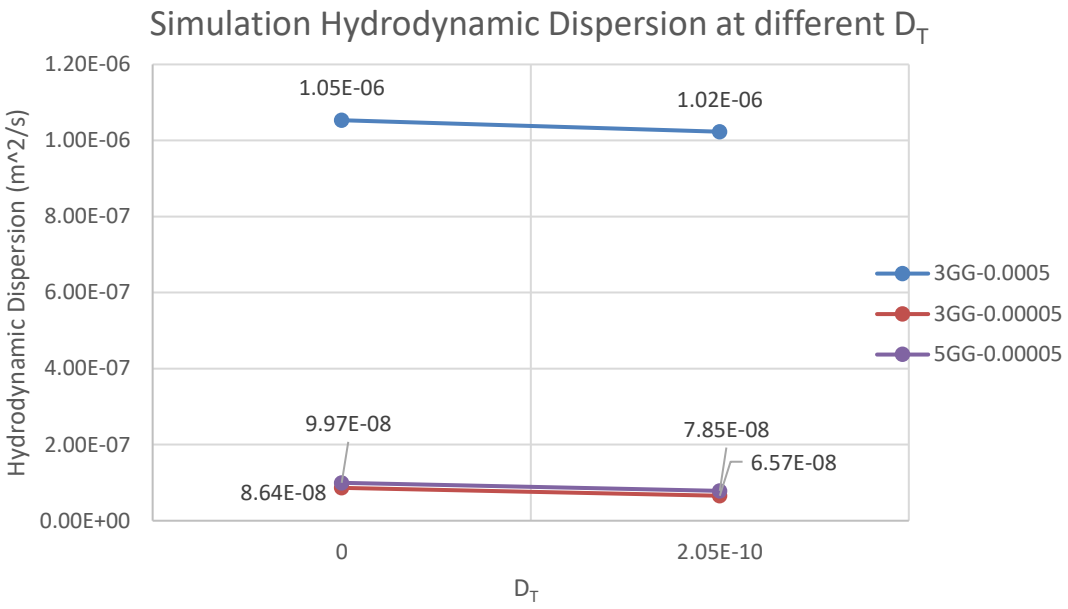

Figure 29. Simulation Hydrodynamic Dispersion at Different D_T

For hydrodynamic dispersion data in ***Figure 29*** at two different molecular diffusion values, the hydrodynamic dispersion at D_T=0 is moderately larger than at D_T=2.05E-10, but they are in the same magnitude. Because the hydrodynamic dispersion has at least two magnitudes of difference with molecular diffusion when v=0.0005m/s and v=0.00005m/s, and given the comparison results between two D_T values, it can be verified that using the D_T value as a constant is reasonable, and the impacts of molecular diffusion are insignificant compare to hydrodynamic dispersion.

Advection-Diffusion Model Fitting

The same advection-diffusion model was fitted to the simulation results shown in

Figure 30.

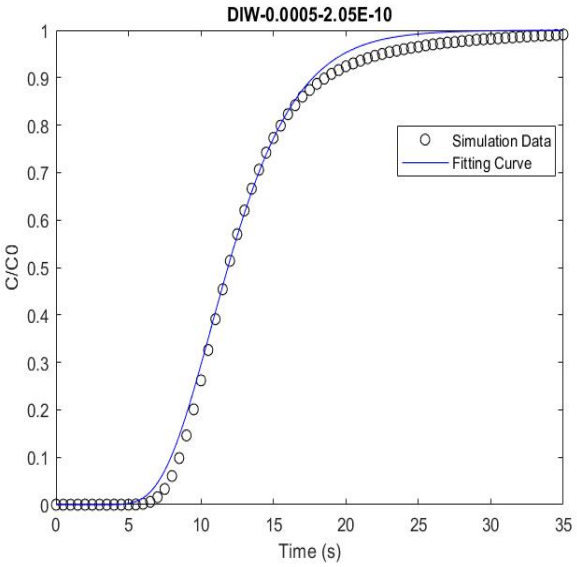

(a) DIW-0.0005m/s-2.05E-10;

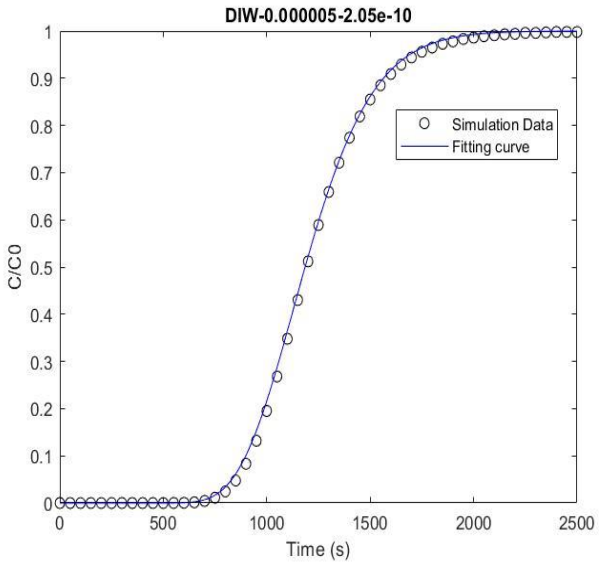

(b) DIW-0.000005m/s-2.05E-10;

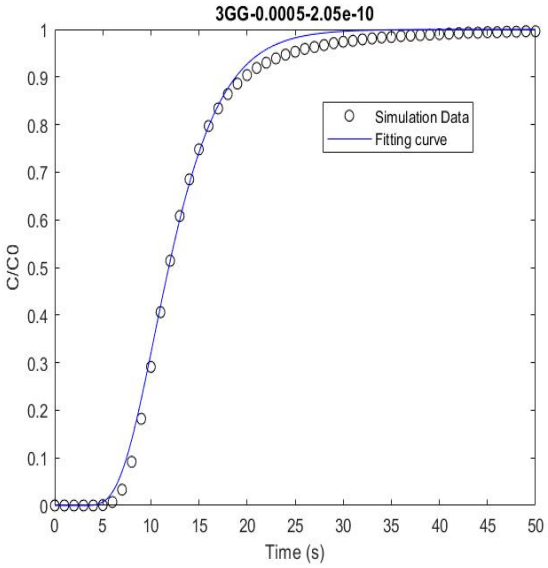

(c) 3GG-0.0005m/s-2.05E-10

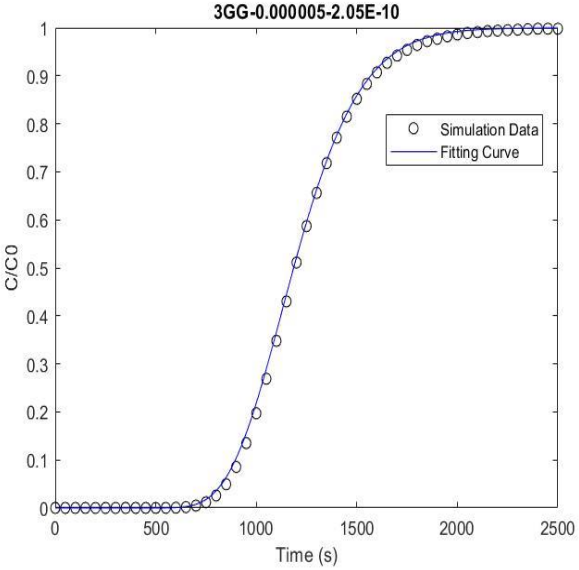

(d) 3GG-0.000005m/s-2.05E-10

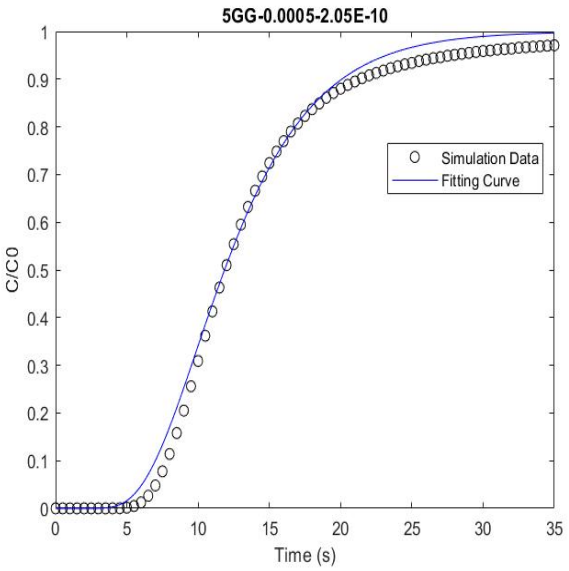

(e) 5GG-0.0005m/s-2.05E-10;

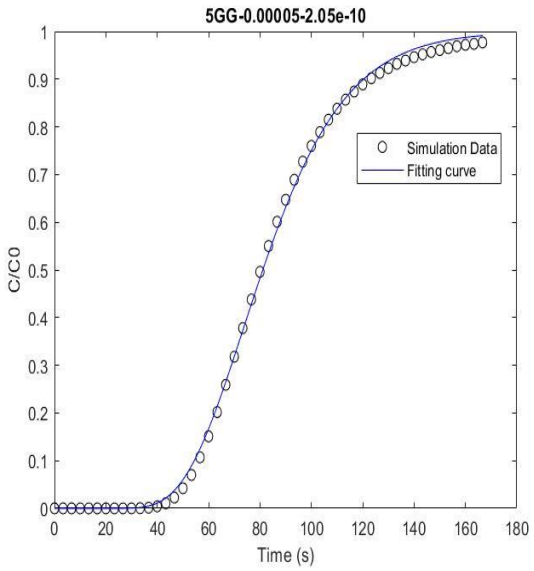

(f) 5GG-0.00005m/s-2.05E-10;

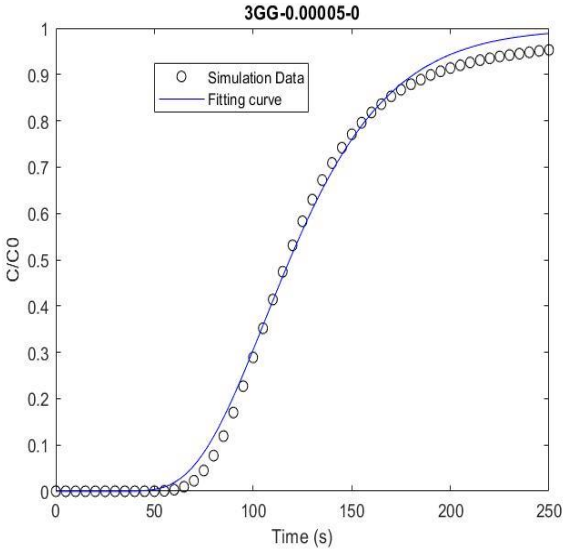

(g) 3GG-0.00005m/s-0;

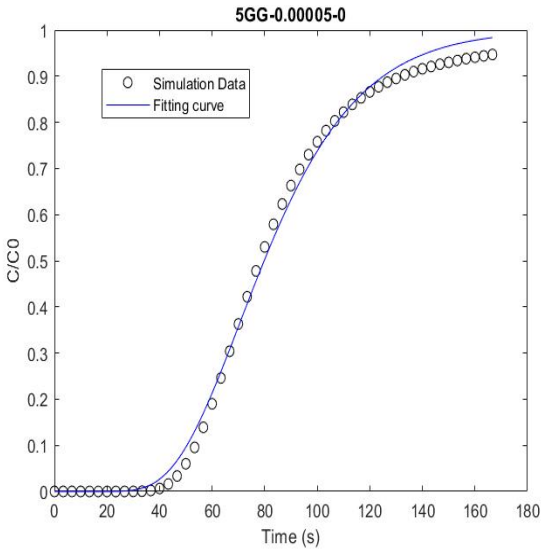

(h) 5GG-0.00005m/s-0

Figure 30. Simulation Breakthrough Curve Fitting

For each fitting curve, the advection-diffusion fitting model does not fit with the simulation breakthrough curve very well, especially when velocity is large. At the smallest velocity we tested, v=0.000005m/s, the difference between the fitting curve

and breakthrough curve is smaller, but still it is not a good match. When D_T=0, the mismatch between fitting model and breakthrough curve is even larger than at D_T=2.05E-10.

If we compare the simulation fitting curve and the breakthrough curve to the experimental fitting curve and the breakthrough curve, the simulation results have longer tails than the experimental curve. Each reaches relative concentration equal to one in a much longer timeframe than the results shown in the experimental data. In the experimental breakthrough curve, $\frac{C}{C_0}$ increases to very close to 1 before PV=1.2, instead of approximately PV=2.5-3 as shown in the simulation breakthrough curves ***Figure 22*** to ***Figure 27***.

This discrepancy is probably because the sample collecting points in the simulation were not in the appropriate place, and the boundary conditions were different. In the advection-diffusion model, the boundary condition is that the gradient of relative concentration reaches zero at infinite distance; however, in the simulation, we put the boundary condition (the gradient of relative concentration equal to zero) right at the outlet of the domain. Because the reservoirs exist, the outlet sample should be collected from a slice of the domain away from the boundary to be equivalent to the advection-diffusion model assumption. The equation to calculate the mass flux in one slice of the domain is listed in ***Eq. (26)***:

$$\frac{< M >_{slice}}{V_{flux}} = \frac{< v_{flux} C >}{v} - \frac{D_m \frac{\partial C}{\partial l}}{v}; \qquad (26)$$

where M is the mass of the slice [M]; v_{flux} is the velocity of the flux; V_{flux} is the volume of the flux; v is Darcy velocity; D_m is molecular diffusion coefficient; and $\frac{\partial C}{\partial x}$ is the concentration change with distance in *l* direction.

Because of the difference between the advection-diffusion model and the computing model, and the longer tails caused by this difference, the experimental results and the simulation are not comparable. The limited computing resources that we have access to also makes the simulation difficult to accomplish. We could not complete the analyze for the slice data in ParaView due to the large size of the data, and lack of resources required to analyze the large amount of data. The simulation for dilute species in non-Newtonian fluids flowing through porous medium is computationally expensive, requiring not only a large amount of computational resources, but also carefully pre-designed models.

Chapter 5. Conclusion

Experimental tracer tests using Newtonian fluids (DIW) and non-Newtonian fluids (0.3% and 0.5% guar gum solution) have shown that hydrodynamic dispersion increases from DIW to guar gum solutions, and increases as the concentration of the guar gum solutions increases. The breakthrough curve fits the advection-diffusion model very well, and the experimental results are repeatable. Although unusual dispersion data appeared in post-DIW, this is due to the difficulty in cleaning the column saturated by guar gum solution, and to the unstable flow caused by the advection between two different types of solutions, DIW and guar gum solutions. The fluctuation within single concentrations of guar gum solutions has been proved by sensitivity analysis to fall within the bounds of the experimental error, and the experimental results are reliable.

In the simulation, we computed REV for different domain systems. Under our limited computing resources, we found that the system reaches steady-state with 4000 spheres, 300^3 blocks, with refinement level equal to 2. With a sphere number smaller than 4000, the pressure drop varies when blocks number grows from 100^3 to 300^3. With a sphere number larger than 4000 spheres and the resolution level greater than 300^3 blocks, the system took longer to get to steady-state, and we observed unstable pressure drop. Eventually, the domain system with 4000 spheres and 300^3 blocks was selected as the domain system applied in scalarTransport. We also found that the refinement level equal to 2 reduces the resolution level significantly for the system to reach REV.

In scalarTransport, we completed most simulations on Dogwood, but could not finish the analysis of the slice of the domain to verify our estimate for the long tails because of limited computing resources. From scalarTransport, we found that the hydrodynamic dispersion decreased in the same order as the velocity decline, which matches the hydrodynamic dispersion function. The simulation hydrodynamic dispersion increases from DIW, to guar gum solutions, and increases when the concentration of guar gum solution rises. When velocity increases, the difference of hydrodynamic dispersion between different fluids is larger. When D_T=0, the hydrodynamic dispersion is slightly larger than D_T=2.05E-10, but the variation is relatively small; because the hydrodynamic dispersion and molecular diffusion have at least two magnitude differences when v=0.0005m/ and v=0.00005m/s, the impacts of molecular diffusion are insignificant.

The scalarTransport simulation breakthrough curve did not match the advection-diffusion model that we used for the entire work. The long tails were observed in each one of the simulations, though we did not get them during the experimental tracer tests. The reason this happened is that the model boundary condition differed between the advection-diffusion model and the OpenFOAM simulation model, as well as the existence of two reservoirs. The boundary condition for the advection-diffusion model is that $grad(\frac{C}{C_0})$ is equal to zero at infinite distance, but the boundary condition in the simulation is that $grad(\frac{C}{C_0})$ is equal to zero at the outlet of the domain. To fix this problem, we can likely sample a slice of the domain away from the boundary to avoid the samples affected by the boundary.

Overall, our experimental work and simulation work indicates a predictively increasing trend of hydrodynamic dispersion for non-Newtonian fluid compared to Newtonian fluids, and an increasing trend when the concentration of non-Newtonian fluids rises, narrowing a small piece of the knowledge gap. However, the simulations did not perfectly match the advection-diffusion model, which caused the experimental and simulation results to be incomparable. More work is needed with fixed simulation models.

Bibliography

1 World Energy Primary Production | Energy Production | Enerdata. [Online]. Available: https://yearbook.enerdata.net/total-energy/world-energy-production.html. [Accessed: 09-Sep-2019]

2 *Statistical Review of World Energy | Energy economics | Home. [Online]. Available: https://www.bp.com/en/global/corporate/energy-economics/statistical-review-of-world-energy.html. [Accessed: 09-Sep-2019]*

3 *Petroleum, natural gas, and coal still dominate U.S. energy consumption - Today in Energy - U.S. Energy Information Administration (EIA). [Online]. Available: https://www.eia.gov/todayinenergy/detail.php?id=36612. [Accessed: 29-Jul-2019]*

4 *Gielen, D. et al. (2019) The role of renewable energy in the global energy transformation. Energy Strategy Reviews 24, 38–50*

5 *Global Energy Outlook 2019: The Next Generation of Energy. [Online]. Available: https://www.rff.org/publications/reports/global-energy-outlook-2019/. [Accessed: 09-Sep-2019]*

6 *Tong, X. et al. (2018) Distribution and potential of global oil and gas resources. Petroleum Exploration and Development 45, 779–789*

7 *Wang, H. et al. (2016) Assessment of global unconventional oil and gas resources. Petroleum Exploration and Development 43, 925–940*

8 *U.S. Crude Oil, Natural Gas, and Natural Gas Proved Reserves, Year-end 2017. [Online]. Available: https://www.eia.gov/naturalgas/crudeoilreserves/. [Accessed: 09-Sep-2019]*

9 *Rahm, D. (2011) Regulating hydraulic fracturing in shale gas plays: The case of Texas. Energy Policy 39, 2974–2981*

10 *EIA adds new play production data to shale gas and tight oil reports - Today in Energy - U.S. Energy Information Administration (EIA). [Online]. Available: https://www.eia.gov/todayinenergy/detail.php?id=38372. [Accessed: 10-Sep-2019]*

11 *NaturalGas.org. [Online]. Available: https://web.archive.org/web/20090503132200/http://www.naturalgas.org/environment/naturalgas.asp. [Accessed: 10-Sep-2019]*

12 *EIA - Annual Energy Outlook 2019. [Online]. Available: https://www.eia.gov/outlooks/aeo/. [Accessed: 29-Jul-2019]*

13 *EPA's Study of Hydraulic Fracturing for Oil and Gas and Its Potential Impact on Drinking Water Resources | US EPA. [Online]. Available:*

https://www.epa.gov/hfstudy. [Accessed: 25-Jun-2019]

14 *Burton, G.A. et al. (2014) Hydraulic "fracking": are surface water impacts an ecological concern? Environ. Toxicol. Chem. 33, 1679–1689*

15 *Vidic, R.D. et al. (2013) Impact of shale gas development on regional water quality. Science 340, 1235009*

16 *Cheng, Y. (2010) , Impact of water dynamics in fractures on the performance of hydraulically fractured wells in gas shale reservoirs. , in SPE International Symposium and Exhibition on Formation Damage Control*

17 *Weltman-Fahs, M. and Taylor, J.M. (2013) Hydraulic fracturing and brook trout habitat in the marcellus shale region: potential impacts and research needs. Fisheries 38, 4–15*

18 *Orangi, A. et al. (2011) , Unconventional Shale Oil and Gas-Condensate Reservoir Production, Impact of Rock, Fluid, and Hydraulic Fractures. , in SPE Hydraulic Fracturing Technology Conference*

19 *Spellman, F.R. (2012) Environmental impacts of hydraulic fracturing, CRC Press.*

20 *Ladd, A.E. (2013) Stakeholder perceptions of socioenvironmental impacts from unconventional natural gas development and hydraulic fracturing in the Haynesville Shale. Journal of Rural Social Sciences*

21 *McBroom, M., ed. (2013) The Effects of Induced Hydraulic Fracturing on the Environment: Commercial Demands vs. Water, Wildlife, and Human Ecosystems, (1st edn) Apple Academic Press.*

22 *Rajagopal, K.R. (1993) Mechanics of non-Newtonian fluids. Pitman Research Notes in Mathematics Series*

23 *Galdi, G.P. and Necas, J. (1993) Recent Developments in Theoretical Fluid Mechanics: Winter School, Paseky, 1992, Illustrated.CRC Press.*

24 *Taylor, G. (1953) Dispersion of Soluble Matter in Solvent Flowing Slowly through a Tube. Proceedings of the Royal Society A: Mathematical, Physical and Engineering Sciences 219, 186–203*

25 *(1954) The dispersion of matter in turbulent flow through a pipe. Proc. R. Soc. Lond. A 223, 446–468*

26 *(1954) Conditions under which dispersion of a solute in a stream of solvent can be used to measure molecular diffusion. Proc. R. Soc. Lond. A 225, 473–477*

27 *Salles, J. et al. (1993) Taylor dispersion in porous media. Determination of the dispersion tensor. Phys. Fluids A 5, 2348–2376*

28 *Auriault, J.L. and Adler, P.M. (1995) Taylor dispersion in porous media: Analysis by multiple scale expansions. Adv. Water Resour. 18, 217–226*

29 *Alizadeh, A. et al. (1980) The theory of the Taylor dispersion technique for liquid diffusivity measurements. Int. J. Thermophys. 1, 243–284*

30 *Bear, J. (1975) Dynamics of fluids in porous media. Soil Sci. 120, 162–163*

31 *Kvenvolden, K.A. (1995) A review of the geochemistry of methane in natural gas hydrate. Org. Geochem. 23, 997–1008*

32 *U.S. energy facts explained - consumption and production - U.S. Energy Information Administration (EIA). [Online]. Available: https://www.eia.gov/energyexplained/us-energy-facts/. [Accessed: 09-Sep-2019]*

33 *Fuel Calorific Values. [Online]. Available: http://cngeurope.com/fuel-calorific-values/. [Accessed: 05-Oct-2019]*

34 *Our Energy Sources, Natural Gas — The National Academies. [Online]. Available: http://needtoknow.nas.edu/energy/energy-sources/fossil-fuels/natural-gas/. [Accessed: 29-Jul-2019]*

35 *Alvarez, R.A. et al. (2012) Greater focus needed on methane leakage from natural gas infrastructure. Proc. Natl. Acad. Sci. USA 109, 6435–6440*

36 *Howarth, R.W. et al. (2011) Methane and the greenhouse-gas footprint of natural gas from shale formations. Clim. Change 106, 679–690*

37 *Natural Gas Is Efficient | IGU. [Online]. Available: https://www.igu.org/natural-gas-efficient. [Accessed: 05-Oct-2019]*

38 *Wang, S. (2018) Shale gas exploitation: Status, problems and prospect. Natural Gas Industry B 5, 60–74*

39 *CISAN-UNAM et al. (2015) Shale Gas in the United States: Transforming Energy Security in the Twenty-first Century. nam 10, 7–38*

40 *Aruga, K. (2016) The U.S. shale gas revolution and its effect on international gas markets. Journal of Unconventional Oil and Gas Resources 14, 1–5*

41 *U.S. Energy Information Administration (EIA) - Natural Gas Data. [Online]. Available: https://www.eia.gov/naturalgas/data.php. [Accessed: 29-Jul-2019]*

42 *Li, Q. et al. (2015) A review on hydraulic fracturing of unconventional reservoir. Petroleum 1, 8–15*

43 *Hydraulically fractured wells provide two-thirds of U.S. natural gas production - Today in Energy - U.S. Energy Information Administration (EIA). [Online]. Available: https://www.eia.gov/todayinenergy/detail.php?id=26112. [Accessed: 25-Jun-2019]*

44 *Hydraulic fracturing accounts for about half of current U.S. crude oil production - Today in Energy - U.S. Energy Information Administration (EIA). [Online]. Available: https://www.eia.gov/todayinenergy/detail.php?id=25372. [Accessed: 25-Jun-*

2019]

45 *Mair, R. et al. (2012) Shale gas extraction in the UK: a review of hydraulic fracturing.*

46 *Lave, R. and Lutz, B. (2014) Hydraulic fracturing: A critical physical geography review. Geography Compass 8, 739–754*

47 *Böhme, G. (1987) Non-Newtonian Fluid Mechanics, Volume 31, 1st Edition.*

48 *Non-Newtonian fluids — Science Learning Hub. [Online]. Available: https://www.sciencelearn.org.nz/resources/1502-non-newtonian-fluids. [Accessed: 08-Oct-2019]*

49 *Non-Newtonian fluid - Wikipedia. [Online]. Available: https://en.wikipedia.org/wiki/Non-Newtonian_fluid. [Accessed: 08-Oct-2019]*

50 *Hayat, T. et al. (2017) Mathematical modeling of non-Newtonian fluid with chemical aspects: A new formulation and results by numerical technique. Colloids and Surfaces A: Physicochemical and Engineering Aspects 518, 263–272*

51 *Hsieh, K.T. and Rajamani, R.K. (1991) Mathematical model of the hydrocyclone based on physics of fluid flow. AIChE J. 37, 735–746*

52 *Hernandez-Morales, B. and Mitchell, A. (1999) Review of mathematical models of fluid flow, heat transfer, and mass transfer in electroslag remelting process. Ironmaking & Steelmaking 26, 423–438*

53 *Bao, K. et al. (2016) , Numerical Modelling of Non-newtonian Fluid Flow in Fractures and Porous Media. , in ECMOR XV - 15th European Conference on the Mathematics of Oil Recovery, Netherlands*

54 *Bear, J. (2007) Hydraulics of Groundwater (Dover Books on Engineering), Dover Publications.*

55 *Landau, L.D. and Lifshitz, E.M. (1958) Statistical Physics (Course of Theoretical Physics vol 5).*

56 *Ostera, H.A. et al. (2007) , Tracing groundwater pollution in the oil industry: myths and reality. , in Latin American & Caribbean Petroleum Engineering Conference*

57 *Abriola, L.M. (1989) Modeling multiphase migration of organic chemicals in groundwater systems--a review and assessment. Environ. Health Perspect. 83, 117–143*

58 *Al-Rashed, M. and Mukhopadhyay, A. (2010) Contamination of groundwater from oil field water disposal pits in Kuwait. Arabian Journal for …*

59 *Myers, T. (2012) Potential Contaminant Pathways from Hydraulically Fractured Shale to Aquifers. Groundwater 50, 872–882*

60 *Vengosh, A. et al. (2014) A critical review of the risks to water resources from unconventional shale gas development and hydraulic fracturing in the United States. Environ. Sci. Technol. 48, 8334–8348*

61 *Smith, M.B. (2015) Hydraulic Fracturing, CRC Press.*

62 *Bear, J. (1979) Hydraulics of groundwater, Illustrated.McGraw-Hill International Book Co.*

63 *Freeze, R.A. and Cherry, J.A. (1979) Groundwater, (1st edn) Prentice Hall.*

64 *Snyder, M.L. and Lichstein, H.C. (1940) Sodium Azide As An Inhibiting Substance for Gram-Negative Bacteria. Journal of Infectious Diseases 67, 113–115*

65 *Lucas, L.L. and Unterweger, M.P. (2000) Comprehensive review and critical evaluation of the half-life of tritium. J Res Natl Inst Stand Technol 105, 541*

66 *C. Hauswirth, S. and A. Bowers, C. Lattice-Boltzmann Modeling and Experimental Study of Non-Newtonian Fluid Flow in Porous Media.*

67 *Mudgil, D. et al. (2014) Guar gum: processing, properties and food applications-A Review. J. Food Sci. Technol. 51, 409–418*

68 *Casas, J.A. et al. (2000) Viscosity of guar gum and xanthan/guar gum mixture solutions. J. Sci. Food Agric. 80, 1722–1727*

69 *Cordes, C. and Kinzelbach, W. (1992) Continuous groundwater velocity fields and path lines in linear, bilinear, and trilinear finite elements. Water Resour. Res. 28, 2903–2911*

70 *Ge, S. (1998) Estimation of groundwater velocity in localized fracture zones from well temperature profiles. Journal of Volcanology and Geothermal Research 84, 93–101*

71 *Novakowski, K. et al. (2006) Measurements of groundwater velocity in discrete rock fractures. J Contam Hydrol 82, 44–60*

72 *APS -APS April Meeting 2019 - Event - Preparation, stability, and performance characteristics of a neutron-sensitive liquid scintillation cocktail . [Online]. Available: https://meetings.aps.org/Meeting/APR19/Session/Z12.7. [Accessed: 05-Nov-2019]*

73 *Reddy, P.J. and Sawant, P.D. (2019) Performance comparison of liquid scintillation cocktails for tritium analysis in environmental and biological samples.*

74 *Bergeron, D.E. et al. (2017) Phase stability and lithium loading capacity in a liquid scintillation cocktail. J. Radioanal. Nucl. Chem. DOI: 10.1007/s10967-017-5341-8*

75 *MANUAL FOR SPHERE PACKING CODE. [Online]. [Accessed: 28-Oct-2019]*

76 *Mcclure, J. Fluid Configurations in a Random Sphere Packing. , Fluid*

Configurations in a Random Sphere Packing. Digital Rocks Portal (April 2016). http://www.digitalrocksportal.org/projects/41. [Online]. Available: http://www.digitalrocksportal.org/projects/41. [Accessed: 11-Nov-2019]

77 *Guide, U. The OpenFOAM Foundation.*

78 *IcoFoam - OpenFOAMWiki. [Online]. Available: https://openfoamwiki.net/index.php/IcoFoam. [Accessed: 23-Nov-2019]*

79 *Temam, R. and Chorin, A. (1978) Navier stokes equations: theory and numerical analysis. J. Appl. Mech. 45, 456–456*

80 *Constantin, P. and Foias, C. (1988) Navier-stokes equations, books.google.com.*

81 *Girault, V. and Raviart, P.-A. (1979) Finite Element Approximation of the Navier-Stokes Equations, 749Springer Berlin Heidelberg.*

82 *PISO algorithm - Wikipedia. [Online]. Available: https://en.wikipedia.org/wiki/PISO_algorithm. [Accessed: 23-Nov-2019]*

83 *Wang, T. et al. (2003) PISO algorithm for unsteady flow field. Journal of hydrodynamics*

84 *J. Oliveira, Raad I. Issa, P. (2001) An improved piso algorithm for the computation of buoyancy-driven flows. Numerical Heat Transfer, Part B: Fundamentals 40, 473–493*

85 *Derivation of the Navier–Stokes equations - Wikipedia. [Online]. Available: https://en.wikipedia.org/wiki/Derivation_of_the_Navier%E2%80%93Stokes_equations. [Accessed: 23-Nov-2019]*

86 *Getting Started on Longleaf - Information Technology Services. [Online]. Available: https://its.unc.edu/research-computing/techdocs/getting-started-on-longleaf/#Job%20Submission. [Accessed: 23-Nov-2019]*

87 *ScalarTransportFoam - OpenFOAMWiki. [Online]. Available: https://openfoamwiki.net/index.php/ScalarTransportFoam. [Accessed: 23-Nov-2019]*

88 *Kim, J.S. et al. (2012) Self-diffusion and viscosity in electrolyte solutions. J. Phys. Chem. B 116, 12007–12013*

89 *Low, K.W.Q. et al. (2016) Pore-Scale Modeling of Non-Newtonian Shear-Thinning Fluids in Blood Oxygenator Design. J Biomech Eng 138, 051001*

90 *Dogwood Cluster - Information Technology Services. [Online]. Available: https://its.unc.edu/research-computing/dogwood-cluster/. [Accessed: 12-Nov-2019]*

91 *Molz, F. (2015) Advection, dispersion, and confusion. Ground Water 53, 348–353*

92 *Ogata, A. (1970) Theory of dispersion in a granular medium. Professional Paper*

93 *Hunter, D.B. and Regan, T. (1972) A note on the evaluation of the complementary error function. Math. Comput. 26, 539–539*

94 *MATLAB - MathWorks - MATLAB & Simulink. [Online]. Available: https://www.mathworks.com/products/matlab.html. [Accessed: 12-Nov-2019]*

95 *Complementary error function - MATLAB erfc. [Online]. Available: https://www.mathworks.com/help/matlab/ref/erfc.html. [Accessed: 11-Nov-2019]*

96 *Darcy, H.P.G. (1856) Les Fontaines publiques de la ville de Dijon. Exposition et application des principes à suivre et des formules à employer dans les questions de distribution d' …, books.google.com.*

97 *Hsu, C.-J. (1981) Numerical heat transfer and fluid flow. Nucl. Sci. Eng. 78, 196–197*

98 *Mydlarski, L. and Warhaft, Z. (1998) Passive scalar statistics in high-Péclet-number grid turbulence. J. Fluid Mech. 358, 135–175*